Journal of Structural Geology

Constraining kinematic and temporal evolution of a normal-sense shear zone: insights into the Simplon Fault Zone (Western Alps)

--Manuscript Draft--

Manuscript Number:	
Article Type:	Original article
Keywords:	Simplon Fault Zone; Ar/Ar geochronology; vorticity; paleopiezometry
Corresponding Author:	Chiara Montemagni, Ph.D. University of Milano–Bicocca: Universita degli Studi di Milano-Bicocca Milano, Milano ITALY
First Author:	Chiara Montemagni, Ph.D.
Order of Authors:	Chiara Montemagni, Ph.D.
	Stefano Zanchetta
Abstract:	The exhumation of the Lepontine Dome in the Central Alps was mainly driven by extensional shear zones at its borders. The Simplon Fault Zone (SFZ), formed as a consequence of east-west lateral extrusion perpendicular to north-south convergence between Adria and Europa plates, has been the leading structure in the exhumation of the western sector of the Lepontine Dome where the deepest rocks of Central Alps are nowadays exposed. We present here a multidisciplinary study of the SFZ combining fieldwork, microstructural analyses, vorticity estimates, quartz c -axis fabric analysis, quartz paleopiezometry and 40 Ar/ 39 Ar geochronology. The SFZ evolved from epidote-amphibolite to greenschist facies and then brittle conditions during shearing. A decrease of simple shear component from 88% to 37% towards the top of the shear zone is observed, with mylonites displaying ages within the 12-8 Ma time interval. Differential stress (60-80 MPa) and strain rate (10 -11 -10 -12 s -1) estimates are in agreement with values obtained for crustal-scale low-angle normal faults developed at medium to shallow crustal levels. Our multiscale and multidisciplinary approach points out that the SFZ experienced a complex evolution, with shear strain heterogeneously distributed across the fault zone in the frame of a decrease of the simple shear component and increase of the differential flow stress toward the top of the shear zone.
Suggested Reviewers:	Eugenio Fazio University of Catania: Universita degli Studi di Catania eugenio.fazio@unict.it
	Hannah Pomella Hannah.Pomella@uibk.ac.at
	Michel Corsini michel.corsini@geoazur.unice.fr
	Koushik Sen koushik.geol@gmail.com
	Claudio Rosenberg claudio.rosenberg@upmc.fr

Dipartimento di Scienze dell'Ambiente e della Terra
Piazza della Scienza 4
I-20126 Milano

UNIVERSITÀ DEGLI STUDI DI MILANO
BICOCCA

Milano, 15 October 2021

Dear Editors,

Please find attached a manuscript by Chiara Montemagni and Stefano Zanchetta for consideration for publication in the *Journal of Structural Geology*. The manuscript is entitled **"Constraining kinematic and temporal evolution of a normal-sense shear zone: insights into the Simplon Fault Zone (Western Alps)"**.

Our manuscript deals with structural and geochronological investigations of the Simplon Fault Zone in the Western Alps and endeavors to constrain its structural and temporal evolution. In this contribution, we combine fieldwork, microstructural analyses (vorticity estimates through different methods, quartz *c*-axis fabric and quartz based paleopiezometer) and ^{40}Ar/^{39}Ar step-heating geochronology. This combination is found to be a useful tool to constrain the timing of shearing and structural evolution of the Simplon Fault Zone, whose history has puzzled researchers for decades as it was responsible for the exhumation of the western Lepontine Dome.

Because our findings develop an integrated methodologic and multidisciplinary approach, they are likely to be of interest to all workers attempting a multidisciplinary investigations of extensional shear zones, of which the Simplon Fault Zone in the western Alps is a prominent example.

We confirm that this manuscript is original and has not been published elsewhere nor is it currently under consideration for publication elsewhere. All authors approved the manuscript and this submission. We hope you could consider our manuscript for publication in *Journal of Structural Geology*.

We appreciate your time and look forward to your response.

Best regards,
Chiara Montemagni

Chiara Montemagni

Constraining kinematic and temporal evolution of a normal-sense shear zone: insights into the Simplon Fault Zone (Western Alps)

Chiara MONTEMAGNI[1,*] and Stefano ZANCHETTA[1]

1: Dipartimento di Scienze dell'Ambiente e della Terra, Università degli Studi di Milano – Bicocca,
Piazza della Scienza 4, 20126, Milano, Italy

E-mail addresses and ORCID:

CM*: chiara.montemagni@unimib.it ; 0000-0002-2850-9744; Tel.: +39 02 6448 2715

SZ: stefano.zanchetta@unimib.it ; 0000-0001-7690-969X

Keywords: Simplon Fault Zone, Ar/Ar geochronology, vorticity, paleopiezometry

Abstract

The exhumation of the Lepontine Dome in the Central Alps was mainly driven by extensional shear zones at its borders. The Simplon Fault Zone (SFZ), formed as a consequence of east-west lateral extrusion perpendicular to north-south convergence between Adria and Europa plates, has been the leading structure in the exhumation of the western sector of the Lepontine Dome where the deepest rocks of Central Alps are nowadays exposed. We present here a multidisciplinary study of the SFZ combining fieldwork, microstructural analyses, vorticity estimates, quartz *c*-axis fabric analysis, quartz paleopiezometry and $^{40}Ar/^{39}Ar$ geochronology. The SFZ evolved from epidote-amphibolite to greenschist facies and then brittle conditions during shearing. A decrease of simple shear component from 88% to 37% towards the top of the shear zone is observed, with mylonites displaying ages within the 12-8 Ma time interval. Differential stress (60-80 MPa) and strain rate (10^{-11}-10^{-12} s^{-1}) estimates are in agreement with values obtained for crustal-scale low-angle normal faults developed at medium to shallow crustal levels.

Our multiscale and multidisciplinary approach points out that the SFZ experienced a complex evolution, with shear strain heterogeneously distributed across the fault zone in the frame of a decrease of the simple shear component and increase of the differential flow stress toward the top of the shear zone.

1. Introduction

Together with the South Tibetan Detachment System in the Himalaya (Caby et al., 1983; Carosi et al., 1998; Law et al., 2004; Iaccarino et al., 2017 and references therein) and the Brenner and Katschberg Normal Faults in the Eastern Alps (Scharf et al., 2016; Rosenberg et al., 2018 and references therein), the Simplon Fault Zone (SFZ) in the Western Alps is one of the most studied low-angle normal faults active in orogenic post-collisional setting (Mancktelow, 1985, 1990, 1992; Grosjean et al., 2004; Steck, 2008; Campani et al., 2010a, 2010b; Massironi et al., 2011; Haertel et al., 2013; Haertel and Herwegh, 2014; Bolognesi and Bistacchi, 2016; Cawood and Platt, 2020). Normal sense shear zones with a dip angle lower than 30° are common in different tectonic settings and accommodate several tens of kilometers of extension (Anderson, 1971; Davis and Lister, 1988; Collettini and Holdsworth, 2004; Collettini et al., 2006; Wernicke, 1981, 2009).

The area of the Simplon Massif in the Central Alps has been studied over a century since the pioneering studies of Studer (1851) and Argand (1916), but it is only from the ’50 (Bearth, 1956) and ’80 (Mancktelow 1985, 1987a,b; Merle et al., 1986; Mancel and Merle, 1987; Steck, 1987) of the past century that the occurrence of a W-SW dipping major extensional detachment fault has been recognized. The SFZ consists of a broad zone (up to ca. 1 km thick) of mylonites overprinted by a narrow (up to 50 m) cataclastic brittle fault at the top (Steck, 1987; Mancktelow, 1985), both of them mainly developed within metagranitoids of the Lower Penninic units.

As quartzofeldspathic rocks could be taken as representative of the upper and middle continental crust (Rudnick and Gao, 2003), the study of large-scale shear zones as the *loci* where deformation localize (Ramsay, 1980) could provide invaluable insights on the rheology of continental lithosphere. The development in space and time of large-scale shear zones is controlled by several factors like *PT* conditions, differential stress, pore fluid pressure, shear sense and time duration of activity (Fossen and Cavalcante, 2017 with references). Such complexity is usually approached by studying microstructures developed at different levels, in different times and at different ambient conditions within a single shear zone (e.g. Stipp et al., 2002; Toy et al., 2008; Law et al., 2013). Quantitative microstructural analyses comprising the determination of grain size distribution, shape preferred orientation (SPO), crystallographic orientation (CPO) and recognition of dominant and relict recrystallization mechanisms in minerals are mandatory for the reconstruction of the shear zone evolution (e.g. Xypolias, 2009, 2010). Such approach could be combined with geochronological dating of minerals that grow or recrystallize during shearing (Sanchez et al., 2011), providing time constraints for the shear zone evolution in space and time and also *PT* conditions of deformation (e.g. Oriolo et al., 2016, 2018; Montemagni et al., 2020, Simonetti et al., 2021).

In this study we investigate through a quantitative approach the evolution of the SFZ in terms of time of activity, microstructures development and distribution across the shear zone, estimate of magnitude and variation of differential flow stress and strain rates during shear zone evolution. Results provide insights on how major extensional detachment fault evolve at middle to upper crustal levels.

2. Geological Setting: the Simplon Fault Zone

The Simplon Fault Zone (SFZ) is a ca. 25° inclined SW-dipping detachment that accommodated orogen-parallel extension during collision between the Adria and Europe plates (Campani et al., 2010b; Mancktelow, 1985; Steck, 2008). The SFZ extends over 30 km between the Ossola valley to the south and the Rhone valley to the north (Fig. 1) . The SW termination of the SFZ is still debated (Steck, 2008; Bolognesi and Bistacchi, 2016): the SFZ could connect with the E-W trending Centovalli Line (Steck, 2008) or with the NE-SW trending Isorno Shear Zone. To the NW the SFZ merges with the dextral E-W Rhone Line (Campani et al., 2010a, Bolognesi and Bistacchi, 2016).

The crustal-scale SFZ detachment accomodated the exhumation of the western portion of the Lepontine Dome of the Central Alps made of tectonic units of the Lower Penninic domain derived from the European passive margin (Steck, 2008 and references within). These Europe-derived units are in contact with the Upper Penninic units forming the hangingwall of the SFZ; such units derive from the Briançonnais microcontinent and from the oceanic and overlying sediments of the Alpine Tethys (e.g. Steck, 2008).

The geometry, kinematics and time of activity of the SFZ, together with its role in the exhumation history of the Lepontine Dome, have been objects of studies since the '50 of the past century (Bearth, 1956; Mancktelow, 1985, 1987a, 1987b, 1990, 1992; Merle et al., 1986; Mancel and Merle, 1987; Steck, 1987, 1990; Steck and Hunzinker, 1994; Grosjean et al., 2004; Keller et al., 2005, 2006; Campani et al. 2010a, 2010b; 2014; Haertel et al., 2013; Haertel and Herwegh, 2014; Bolognesi and Bistacchi, 2016; Bergemann et al., 2020; Cawood and Platt, 2020).

The SFZ shows an asymmetric structure: the hanging wall displays evidences of brittle deformations, whereas the footwall (corresponding to tectonic units forming the Toce Dome, the western subdome of the Lepontine one; Steck, 2008; Elfert et al., 2013) exhibits syn-exhumation ductile deformations resulting in ca. 1-2 km of mylonites (Mancktelow, 1985) developed at epidote amphibolite to greenschist facies conditions from lower to upper structural levels, respectively (Mancktelow, 1992; Campani et al., 2010a). High temperature mylonites correspond to *zone 1* in Bolognesi and Bistacchi (2016), whereas low-temperature mylonites correspond to *zone 2*. The discrete boundary dividing the hangingwall from the footwall consists of the Simplon Line (SL), a narrow (10-15 m thick, Bolognesi and Bistacchi, 2016) fault zone corresponding to a brittle detachment that marks the last structural evolution stage of the SFZ (e.g. Bearth, 1972; Mancktelow, 1992; Bolognesi and Bistacchi, 2016). Outside the fault core of the SL, the brittle damage zone extends for others 30-40 m in the footwall. The SL was interpreted to be late Miocene as it crosscuts the Glishorn and Berisal back folds in the northern part of the footwall related to the exhumation of the Aar Massif (Campani et al. 2010a). The footwall of the SFZ consists of a wide zone (Mancktelow, 1985, 1992) of mylonites referred to as Simplon Shear Zone (SSZ; Campani et al., 2010a; Cawood and Platt, 2020).

Within the mylonites of the SSZ shear sense indicators (SC' fabric, K-feldspar porphyroclasts, quartz grain shape preferred orientation; Mancktelow, 1985; Cawood and Platt, 2020) are diffused both at the meso and the microscale, pointing to a top-to-the-SW sense of shear.
The shearing deformation and related exhumation of the Lower Penninic units along the SSZ has been constrained by a wealth of geo- and thermo-chronometric data (i.e. K/Ar, ^{40}Ar/^{39}Ar, Rb/Sr, Fission Track analysis on Apatite and Zircon) resulting in a wide range of ages, from 35-30 (Steck and Hunzinker, 1994) to 3 Ma (Grasemann and Mancketlow, 1993; Campani et al., 2010a, 2010b). An in-depth review of the thermo- and geochronological dataset has been reported by Campani et al. (2010a and references therein) who highlighted that ages are concordantly holder in the hanging wall with respect to the footwall of the SL, suggesting that the SSZ was active under ductile deformation regime at least since 20 Ma (30-35 Ma following Steck and Hunzinker, 1994) and the subsequent ductile-to-brittle transition (280-300 °C) occurred between 14.5 and 10 Ma (Campani et al., 2014).

3. Structural analysis

3.1 Field mapping and sampling

Mylonites and centimeter-thick bands of ultramylonites developed in the SSZ show a transition from epidote amphibolite to greenschist facies conditions moving structurally upward, i.e. from the bottom of the shear zone toward the brittle SL. Quartz recrystallization microstructures (Mancktelow, 1985; Cawood and Platt, 2020), together with geothermometric data (Cawood and Platt, 2020 and references therein) describe this transition.
Geological and structural mapping performed at the 1:5000 scale in the Simplon Pass area and to the south, resulted in the production of a detailed geological-structural map (Fig. 2) that has been used as a background for further sampling and structural analysis.
The architecture of the shear zone displays a non-linear deformation gradient, with protomylonites (*sensu* Sibson, 1977) developed both within the Monte Leone and Berisal orthogneisses and mylonites and ultramylonites mainly developed within rocks of the Berisal Unit, in the upper levels of the SSZ. Repeated transitions from protomylonitic to ultramylonitic fabric is frequently observable in the field (Fig. 4) at the outcrop scale. Approaching the SL, i.e. passing from *zone 2* to *zone 3* of Bolognesi and Bistacchi (2016), a second spaced mylonitic foliation (Fig. 4; Sm_2 in Mancktelow, 1992; Campani et al., 2014; Cawood and Platt, 2020) crosscuts the older one (Sm_1). Sm_2 resulted from the progressive interfingering and merging of discrete shear zones that are not pervasive away from the SL and become increasingly diffused approaching the SL in *zone 3* of Bolognesi and Bistacchi (2016), broadly corresponding to the "low-T mylonites" zone of Cawood and Platt (2020).
The Sm_1 mylonitic foliation dips SW to WSW in the Berisal Unit (Figs. 2 and 3) and WSW to W in the Monte Leone Unit (265°N and dip angle of 25°), displaying a slight clockwise rotation approaching the SL. The attitude of stretching lineation appears to be more constant, with a trend clustering around 240°N and plunge of ca. 20° (Fig. 2). SC' fabric is frequently developed within mylonites derived from the Berisal orthogneiss (Fig. 4).
Even if a general increase of the shear strain have been previously described from the bottom to the top of the SSZ approaching the SL (Haertel and Herwegh, 2014), our observations revealed that shear strain appears to be unevenly distributed across the ca. 600 m thick mylonitic zone of the studied transect (Fig. 4e-f). Ultramylonites occur as several decimeters up to 2-3 m thick bands within mylonites and protomylonites derived from the Berisal orthogneiss. The transition from protomylonites to ultramylonites occur in a few decimeters (Fig. 4e-f). The heterogeneous shear strain

distribution could be related to a complex evolution of the SSZ, not directly associable to typical evolution models of shear zones (Fossen and Cavalcante, 2017).

In order to evaluate the kinematic vorticity of flow across the SSZ we chose to study sheared quartz veins occurring within mylonites of the SSZ (Haertel and Herwegh, 2014) and mylonitic and ultramylonitic orthogneiss samples. Due to the occurrence of the Sm_2 second mylonitic foliation approaching the brittle SL, we carefully selected outcrops within the SSZ where the SC' fabric is unequivocally related to the first stage of shearing (i.e. Sm_1). In order to prove the efficacy of our approach we dated by the $^{40}Ar/^{39}Ar$ method syn-mylonitic micas along both S and C' planes for each sample used for vorticity estimates (see section 4.2 for details).

3.2 Microstructures, petrography

We describe an alternating transition from mylonites to ultramylonites with a non-linear deformation gradient. From the bottom to the top of the SSZ (Figs. 3 and 5), quartz recrystallization microstructures show an overall transition from high-to-low temperature mechanisms expressed by Grain Boundary Migration (GBM), Subgrain Rotation (SGR) and Bulging (BLG) recrystallization mechanisms (Stipp et al. 2002; Passchier and Trouw, 2005).

Kinematic indicators as a well-developed SC' fabric, σ/δ-type K-feldspar porphyroclasts, oblique foliation in quartz definitely point to a top-to-SW sense of shear.

A structural transect (Fig. 3) from bottom to top of the SSZ allow to observe different paragenesis and recrystallization mechanisms operating at different *PT* conditions. All thin sections were cut parallel to lineation and perpendicular to foliation, in order to observe structures on XZ plane of the finite strain ellipsoid.

Starting from the bottom of the SSZ, in paragneiss (Fig. 5g) quartz is strongly elongated in ribbons that, according to Passchier and Trouw (2005) and Trouw et al. (2010), contain single elongated crystals probably formed by GBM, nevertheless core and mantle structures distinctive of SGR recrystallization mechanism (Passchier and Trouw, 2005) occur in some domains. Oblique foliation in quartz clearly indicates a top-to-SW shear sense (Fig. 5g).

Moving structurally upward in mylonitic orthogneiss a bimodal quartz grain distribution is present with GBM dominating over SGR and *vice versa*, with these mechanisms alternating in becoming the prevailing quartz recrystallization mechanism (Fig. 5f). SC' fabric entirely occurs along the structural transect with biotite and chlorite (re)-crystallizing along C' planes (Fig. 5c-f). Synthetic bookshelf structures in K-feldspar (Fig. 5e) are interpreted to be characteristic of low to medium temperature of deformation (400-500 °C; Pryer, 1993; Passchier and Trouw, 2005 and references therein) in agreement with quartz recrystallization microstructures. Approaching the SL, BLG appears but SGR remains the dominant quartz recrystallization mechanism as the transition to new grains is gradational (Fig. 5c-d; Passchier and Trouw, 2005; Trouw et al., 2010). At the top of the SSZ, sheared quartz veins are characterized by oblique foliation and SGR recrystallization mechanism (Fig. 5a-b). The observed quartz recrystallization features are similar to those described by Mancktelow (1992) and Haertel and Herwegh (2014), who reported predominant and advanced SGR and GBM with increasing distance from the SL.

3.3 CPO and vorticity analyses

In order to quantitatively assess the crystallographic preferred orientation (CPO) of mylonite and ultramylonite, the quartz *c*-axis fabric has been measured through a Zeiss FEG-SEM Gemini 500 equipped with a QUANTAX EBSD at *Piattaforma di Microscopia*, Università degli Studi di Milano – Bicocca.

Crystal fabric data were acquired on thin sections cut perpendicular to foliation and parallel to lineation, representing the XZ plane of the finite strain ellipsoid. EBSD analyses were performed on graphite coated (ca. 4 nm in thickness) thin sections polished with colloidal silica. Microscope setup was 20 keV of accelerating voltage and 15 nA of beam current. Acquisition resolutions varied from 0.75 µm/pixel to 2.08 µm/pixel. Grain boundary maps obtained by EBSD assisted analysis have been used to quantify grain size (equivalent circular diameter) distributions (Fig. 6h-m).

At high levels of shear strain, quartz microstructures like grain size, shape preferred orientation (SPO) and CPO record the last stage of steady state deformation (i.e. Means, 1981, 1995; Haertel and Herwegh, 2014). It is widely accepted that quartz CPO depends on temperature, strain rate, water content and differential stress (Lister, 1977; Stipp et al., 2002; Menegon et al., 2008; Pennacchioni et al., 2010; Peternell et al., 2010). The temperature of deformation controls the intra crystalline slip systems, with activation of basal <a>, rhomb <a>, prism <a> and prism <c> slip systems with increasing temperature (Lister and Paterson, 1979; Pennacchioni et al., 2010). Studying the quartz CPO, microstructures and grain size distribution, thus provide tools to investigate the differential stress and strain rates that conditioned the evolution of the shear zone.

Another aspect that could be probed by studying microstructures developed at different structural sites within a shear zone is the kinematic of the flow (e.g. Law, 2010). The kinematic vorticity number W_k indicates the amount of rotation relative to the amount of stretching at a single point in space at time (*t*) during deformation (Malvern, 1969; Iacopini et al., 2011). W_k thus represents basic flow parameters describing the kinematic of flow in order to distinguish the relative amount of pure and simple shear within a shear zone. The W_k is 1 for simple shear and 0 for pure shear and between 0 and 1 for general shear flow (Passchier, 1987; Fossen, 2010).

Several methods have been developed over the years to obtain kinematic vorticity estimates through a thin section based analysis: shear bands or SC' (Kurz and Northrup, 2008; Gillam et al., 2013), rigid porphyroclasts (Wallis et al., 1993; Jessup et al., 2007) and oblique grain-shape foliation (Law, 2010; Xypolias, 2010 and references therein) methods are just some of them.

Shear bands method (Kurz and Northrup, 2008; Gillam et al., 2013) is based on the orientation of C' planes with respect to the shear zone boundary. In any type of flow, it is possible to recognize two lines, defined as flow apophyses (A_1 and A_2), along which the particles do not undergo rotation. The lower the angle between the two apophyses the lower the simple shear component, as the flow apophyses are parallel each other in simple shear, perpendicular in pure shear and form an acute angle in the direction of the flow in a general shear flow. The C' plane is the bisector of the angle 2θ between the flow apophyses: the vorticity number can be derived through the equation $W_m = \cos 2\theta$ (Kurz and Northrup, 2008), where θ is the angle between C' and shear plane that is assumed to be parallel to the flow apophysis A_2 (Kurz and Northrup, 2008; Gillam et al., 2013).

Vorticity estimates based on the rigid porphyroclasts method (Wallis et al., 1993; Jessup et al., 2007) relies on the fact that in a general shear flow porphyroclasts are partitioned into two populations: one rotates continuously and therefore does not develop a preferred orientation, the other aligns along a minimum energy position (Jessup et al., 2007). Parameters that allow to obtain the kinematic vorticity number are a and b axes of the clast, which define its aspect ratio, and the angle θ between the a-axis and the trend of the main foliation in the sample (Wallis et al., 1993). Vorticity is uniquely defined by aspect ratio and θ. Oblique grain-shape foliation method (Law, 2010; Xypolias, 2010) is based on the measurement of the angle between the oblique foliation and the shear zone boundary, that should be equal to the angle between the A_2 and the extensional ISA_2 (Xypolias, 2010) and, as the quartz *c*-axis re-oriented due to the last increment of ductile deformation, this method estimates the final increase (W_n) of ductile deformation (Wallis, 1995). Therefore the vorticity number can be obtained from $W_n = \sin2(\delta+\beta)$, where δ is the maximum angle between the main and oblique foliation and β is the angle between the shear plane and the main foliation measured from the quartz *c*-axis fabric (Xypolias, 2010).

The results of quartz *c*-axis fabric and vorticity estimates, inverse pole figure maps (IPFmaps) colour coded with respect to the X direction and grain size distributions are reported in Figure 6; *a*-axes fabrics in Supplementary Figure 1.

Quartz *c*-axis distributions (Fig. 6) are characterized by single girdle and type-I cross girdle of Lister (1977) and probably by a transition between single and cross girdle (Fig. 6b). These textures suggest a medium-low *T* of deformation. In general, Y maximum fabrics have been observed with lesser concentration of *c*-axes close to the Z axes (Fig. 6a-d). All patterns show an anticlockwise asymmetry with respect to the XZ plane. Rhomb <a>, prism <a>, ± basal <a> are the active slip systems (Fig. 7; Schmid and Casey, 1986). As discussed in Toy et al. (2008) based on relationship between the position of *c*-axis maxima on a stereographic projection and associated slip planes reported by Schmid and Casey (1986), Y maxima fabrics are the result of dominantly prism <a> slip, whereas type-I cross girdle fabrics derived from a combined basal <a> and prism <a> slip in plane strain (k=1) conditions. If *c*-axes maxima are between Z and Y axes the prevailing slip is ±rhomb <a>.

Oblique grain shape foliation method reveal high vorticity number ranging between 0.67 and 0.97 resulting in simple shear component from 48% to 88%. In agreement with field evidences and microstructural observations, R_{xz} values (Fig. 6e) are heterogeneously distributed within the shear zone, showing higher values within ultramylonite bands and close to them, reflecting higher finite shear strain values.

Vorticity estimates through the SC' method (Fig. 7a-b) suggest a clear decrease in W_m from lower (sample SPL-3, Figs. 2, 4d and 7b) to upper structural level of the SSZ (sample SPL-7, Engiloch, Figs. 2, 4f and 7a). Indeed W_m ranges from 0.83 to 0.59, corresponding to 62% and 41% of simple shear component, respectively. In order to select the proper value of the angle θ to calculate the W_m, we follow the interpretation of Gillam et al. (2013).

RGN method provided lower W_m (Fig. 7c-d) resulting in lower simple shear components of 37-42% (W_m = 0.53-0.61; sample SPL-3; Fig. 7d) and 40-41% (W_m = 0.55-0.60; sample SPL-7; Fig. 7c) for bottom and top of the shear zone, respectively.

3.4 Quartz paleopiezometry and strain rate

Four samples (Fig. 6; SPL-20, SPL-6, SPL-2 and SPL-5) from SSZ have been selected for quartz paleopiezometry in order to determine the magnitude of the differential flow stress (Behr and Platt, 2011; Menegon et al., 2011). We carefully avoided samples in which quartz is recrystallized especially *via* GBM as flow stress could be underestimated as extensively discussed in Stipp et al. (2010). In our case GBM is the dominant recrystallization mechanism in quartz in samples coming from the structurally lower part of the SSZ (Fig. 3). The grain size distribution of analysed quartz samples has been obtained through EBSD data and expressed as arithmetic mean following Ghosh et al. (2016). Grain size is expressed as equivalent circular diameter (D_m). Grain size distributions have been then used to estimate the differential stress (σ_1-σ_3) during the shearing activity of the SSZ. We applied the piezometer proposed by Stipp and Tullis (2003) for the recrystallization regime 2/3 corrected with the experimental calibration of Holyoke and Kronenberg (2010): $D=2451(\sigma_1-\sigma_3)^{-1.26}$, where D is the average recrystallized grain diameter. The obtained values (Fig. 6) are D =10.12 ± 5.56 μm and (σ_1-σ_3) = 78 ± 23 MPa for SPL-20, D =12.28 ± 6.48 μm and (σ_1-σ_3) = 67 ± 19 MPa for SPL-6, D =12.26 ± 5.30 μm and (σ_1-σ_3) =67 ± 17 MPa for SPL-2, D =14.30 ± 6.51 μm and (σ_1-σ_3)

= 59 ± 15 MPa for SPL-5, showing an increase in differential stress towards the brittle SL. Nevertheless, it is worth to note that all calculated differential stress values are partially overlapping considering errors mainly derived from the grain size analysis.

Strain rates ($\dot{\varepsilon}$) have been estimated through the wet-quartzite flow law of Hirth et al. (2001): $\dot{\varepsilon}=A\sigma^{n}(fH_2O)^{m}e^{-Q/RT}$, where A, n and m are parameters calculated experimentally, Q is the activation energy, R is the ideal gas constant, fH_2O is the water fugacity calculated using the equation of state reported in Pitzer and Sterner (1994) for *T* in the range 420-500 °C and *P* 0.4-0.5 GPa consistently with quartz recrystallization mechanisms and other published *T* and *P* estimates (e.g. Haertel and Herwegh, 2014; Cawood and Platt, 2020). The estimated strain rate values are between 10^{-12} and 10^{-11} s^{-1} (Fig. 10).

4. Geochronological dating of SSZ activity

In order to constrain the SSZ activity we performed $^{40}Ar/^{39}Ar$ stepwise heating analyses on selected samples from the structural transect of the SSZ described above (Fig. 3) with known chemical composition of micas (Fig. 8 and Supplementary Table 1).

4.1 Microprobe analyses

Quantitative chemical analyses of muscovite and biotite were performed on graphite-coated thin sections on a total of 50 points, with a JEOL 8200 SuperProbe EMP at Dipartimento di Scienze della Terra “A. Desio”, Università degli Studi di Milano, using 3 µm spot size, 15 kV acceleration voltage, 5 nA current and a counting time for each analysis of 30 s on the peaks and 10 s on backgrounds. Natural silicates and oxides has been used as standards. Analyses (Fig. 8 and Supplementary Table 1) were recalculated as atoms per formula unit (apfu) based on 11 oxygens.

Both micas along the main foliation and along C’ planes have been analysed. No significant differences in terms of composition have been observed between the two microstructural positions (Fig. 8). Muscovite (SPL-1, SPL-3, SPL-4, SPL-6 and SPL-8) shows a variable degree of phengitic substitution with Si concentration varying between 2.90 and 3.40 (apfu) and a Na/(Na+K) content (Guidotti and Sassi, 1998) mostly ranging between 0.01 and 0.04. Biotite (SPL-1 and SPL-4) has low Ti concentration (0.06-0.14 apfu).

4.2 $^{40}Ar/^{39}Ar$ geochronology

Micas were carefully microdrilled directly on thins sections, both from the main mylonitic foliation and C’ planes, and attentively hand-picked. Separated micas were cleaned in ultrasonic baths of acetone and pure water.

The double dating of both micas stable on the S and C’ planes is needed to demonstrate that the vorticity estimates based on SC’ were based on effectively coeval fabric and not to reactivated planes or newly formed ones, as the second generation of mylonitic foliation (Sm_2; Mancktelow, 1992) observable close to the brittle SL. Samples and standards were irradiated in the McMaster University reactor (Ontario, Canada) for 10 MWh, accurately avoiding Cd shielding. Standard of McClure Mountain hornblende (MMhb) has an assumed age of 523.98 ± 0.12 Ma (Schoene and Bowring, 2006). Stepwise heating experiments were performed in a double-vacuum furnace of “Dipartimento di Scienze dell’Ambiente e della Terra, Università degli Studi di Milano – Bicocca” and samples were heated in 12 steps for ca. 20 min each following the analytical approach reported in Montemagni and Villa (2021).

All the gas release patterns (i.e. the differential release and the age spectrum) display similar features (Fig. 9 and Supplementary Table 2). The flat part of the age spectrum, occurring for all the sample at steps 3-4, corresponds to homogeneous and lowest Ca/K values and the degassing peak in the Ar Differential Release Plot (DRP). The comparison between the Ca/K ratios (derived from the ^{37}Ar/^{39}Ar ratios), the DRP and the apparent age spectra suggests that for all samples the Ar isotopic data can be interpreted as gas release from different mineral reservoirs, micas and feldspars, and from their mixtures (Müller et al., 2002; Vance et al., 2003; Villa et al., 2000). The age of the mylonitic foliation (Fig. 9) ranges between 9.23 ± 0.24 Ma and 8.09 ± 0.04 Ma from bottom to top of the SSZ, respectively, with the oldest age of 11.70 ± 0.23 occurring in the middle of the sampling transect (Fig. 10). As testified by fieldwork and microstructures analyses, the shear strain distribution within the SSZ is heterogeneous, with narrow sectors of the broad mylonitic zone that could be re-activated or have protracted their activity for longer time with respect to others. The main consequence of these features is the age of the mylonitic foliation that do not reflect a straight pattern of younging ages approaching the top of the SSZ.

5. Discussion

5.1 Deformation of the SSZ

The SSZ is a gently dipping top-to-the-SW normal sense shear zone, with the main mylonitic foliation and lineation in the Simplon Pass area and immediately to the south of it constantly dipping towards W-SW. It developed under conditions of decreasing *PT* moving structurally upward from epidote amphibolite to greenschist facies conditions during the exhumation, as suggested by the occurrence of stable syn-kinematic mineral assemblage of epidote + biotite, biotite + white mica, white mica + chlorite, together with the deformation temperature suggested by quartz recrystallization mechanisms. The deformation gradient is non-linear with proto-, ultra- and mylonites alternating in the SSZ, as suggested by field work and microstructural observations.

Kinematic vorticity data using the three methods described above suggested that the coaxial component (i.e. the pure shear percentage) of the flow increases moving structurally upwards, with deeper structural levels characterized by higher W_m reflecting a higher simple shear component. Estimated W_m values varies between 0.53 and 0.97, depending on structural position and analytical method. Rigid porphyroclasts methods systematically yielded much lower values with respect to SC' and oblique grain shape foliation methods. The differences in vorticity estimates using rigid porphyroclasts and oblique grain shape foliation methods have been deeply investigated by Law et al. (2004, 2013), Johnson et al. (2009) and Law (2010) who suggested that analytical problems, different recorded parts of deformation history, non-steady flow, spatial partitioning of W_m, clast lubrication and strain localization at clast margins could be just some of the critical issues. Despite these issues that suggest caution in directly correlating the vorticity estimates to the coaxial *vs* non-coaxial component of shear deformation, the pattern we obtained coherently displays that the proportion of simple shear increases structurally downwards, ranging from 37% in the top to 88% in the bottom of the SSZ. R_{xz} values, inferred from mylonites, are heterogeneously distributed within the shear zone suggesting that different portions of the SSZ accommodated different amount of finite strain, as already suggested by field and microstructural observations.

5.2 Age of deformation and structural evolution of the SSZ

A detailed summary of all previously geochronological data is reported in Campani et al. (2010a), who summarized the dataset of ages obtained through different geochronometers. Such ages have been generally interpreted as "cooling ages" and consequently controversial interpretations arose due to lack of petrological and microstructural constraints (i.e. Villa, 2016).

New ^{40}Ar/^{39}Ar chronological data coupled with vorticity analyses led us to precisely depict the evolution of the SSZ by providing constraints on the main stages of shearing.

Our ^{40}Ar/^{39}Ar data on micas implied that ductile shearing along the SSZ was still ongoing at 8 Ma in the upper part of the shear zone where such ages have been recorded by micas along the SC' ductile fabric (Fig.10). Therefore brittle-ductile transition, at least in the upper SSZ, occurred after 8 Ma contrary to what inferred by Campani et al. (2010a), who suggested that brittle-ductile transition occurred between 14.5 and 10 Ma. ZFT ages in the Simplon Pass area ranges between 9 and 13 Ma (Campani et al., 2010a), coeval within error to our ^{40}Ar/^{39}Ar data (ca. 8-12 Ma). This overlap suggests that the transition from near 500 °C of ambient temperature to <250 °C occurred in a very short time span, in turn pointing to very fast exhumation rates for the footwall units of the SFZ during this time interval. Grasemann and Mancktelow (1993) suggested that in the time span 18-15 Ma the SFZ underwent its most active period, although a continuation up to 5 Ma is plausible. Ages approaching 10 Ma for ductile deformation in the footwall of the SL were already proposed also by Hunziker and Bearth (1969) who dated (Rb/Sr method) at 11 Ma, interpreting these data as "cooling ages".

According to quartz recrystallization mechanisms, temperature of deformation ranges between 390 and 530 °C, as the predominant recrystallization mechanism is SGR (Stipp et al., 2002). This range is coherent with deformation temperature comprised between 400 and 500 °C inferred from K-feldspars microstructures (see section 3.2). These temperature are also in agreement with *PT* estimates of Haertel et al. (2013) and Cawood and Platt (2020) who suggested 490 °C as maximum temperature of deformation in the lower part of the SSZ.

Maximum temperature of deformation has been recorded by structurally lowermost samples (SPL-4 and SPL-5; Figs. 3 and 10) in which quartz is characterized by GBM recrystallization mechanisms that is likely to occur above 530 °C (Stipp et al., 2002).

All these data point out that the SSZ was active at middle to shallow crustal levels in a time span of several Myrs. The study of the kinematic evolution and deformation history of the SSZ could provide invaluable insights on the mechanical behaviour of the middle and upper continental crust (e.g. Hacker et al., 1992) with special regards to the calculation of the magnitude of the differential flow stress and associated strain rates.

Differential stress and strain rate estimates have been obtained through time for several ductile normal-sense shear zones (e.g. Hacker et al., 1990, 1992), transpressive shear zones (e.g. Ceccato et al., 2018; Graziani et al., 2020; Simonetti et al., 2021) and thrust-sense shear zone (e.g. Law et al., 2013; Bose and Mukherjee, 2020) all developed at middle to upper crustal level. Obtained values of differential stress range from a few tens of MPa to more than 150 MPa, with strain rates usually in the order of 10^{-18} s^{-1} to 10^{-11} s^{-1}. Focusing on normal-sense shear zones, Hacker et al. (1990, 1992) obtained differential flow stresses of 40-150 MPa and strain rates faster than 10^{-14} s^{-1} for the low-angle Whipple Mountains detachment fault (SE California, US), one of the larger extensional detachments responsible for the exhumation of metamorphic core complexes in the southwestern U.S. Cordillera (Davis and Lister, 1988). Our strain rate estimates obtained on sheared quartz veins within the SSZ mylonites are well within the range observed for shear zones cited above. Strain rates are in the order of 10^{-12} s^{-1} and 10^{-11} s^{-1}, with slightly higher strain rates recorded at the bottom of the SSZ, coupled with the highest temperatures (ca. 500 °C) of deformation and the highest simple shear component in the kinematic vorticity of flow (W_m=0.97, Fig.10). Unlike strain rates remain nearly constant across the SSZ, the differential flow stress changes from ca. 60 MPa at the bottom to ca. 80 MPa near the brittle SL, coupled with a progressive increase in the pure shear component. Such pattern is likely linked to the diminishing of the temperature of deformation approaching the brittle fault plane of the SL, considering a broadly constant strain rate across the entire shear zone through time, or at least during the 12-8 Ma time interval. The fact that strain rates remains constant is a clue for a non-isothermal deformation because in this case strain rates are expected to increase toward the fault plane (e.g. Austin et al., 2008). On the other hand, the results obtained through the vorticity analysis on the studied transect are partially discordant to those obtained in other sector of the SSZ, where strain localization with a progressive increase of the simple shear component towards the fault plane have been described (Haertel and Herwegh, 2014). The absence of a significant strain localization in the transect that we have studied could arise from the heterogeneous distribution of shear strain we observed in the field. Moreover, the lack of a linear gradient for the age of deformation, as suggested by ^{40}Ar/^{39}Ar data on syn-mylonitic micas (Figs. 9 and 10), suggests a complex spatial evolution pattern, with shear deformation that was concentrated trough time at different levels of the SSZ, not following a single younging direction across the shear zone.

6. Conclusions

The evolution of the SSZ has been kinematically and temporally constrained applying a multidisciplinary and multiscale approach. The results allow us to infer the deformation regime during the time span of SSZ shearing activity. The SSZ formed initially at epidote-amphibolite facies conditions and then evolved towards greenschist facies conditions during shearing up to reach brittle conditions along the narrow SL. ^{40}Ar/^{39}Ar geochronology on micas recrystallized along ductile mylonitic fabric revealed that shearing was active mainly between ca. 12 and 8 Ma in the studied transect. Kinematic evolution of the SSZ has been constrained through kinematic vorticity estimates to evolved towards dominated pure shear component towards the top of the shear zone. The application of several independent methods for evaluating the kinematic history is recommended in order obtain more realistic estimates. The calculated differential stress and strain rate are in agreement with those obtained for crustal-scale low-angle normal faults evolved at middle to upper crustal levels.

Acknowledgments

This research was funded by Dipartimento di Scienze dell'Ambiente e della Terra, Università degli Studi di Milano – Bicocca (S. Zanchetta). We thank A. Risplendente (Università degli Studi di Milano) for his support during the electron microprobe analyses.

References

Anderson, R.E., 1971. Thin-skin distention in the Tertiary rock of southwestern Nevada. Geol. Soc. Am. Bull. 82, 43-58. https://doi.org/10.1130/0016-7606(1971)82%5B43:TSDITR%5D2.0.CO;2.

Argand, E., 1916: Sur l'arc des Alpes Occidentales. Eclogae Geol. Helv. 14, 145-204.

Austin, N., Evans, B., Herwegh, M., Ebert, A., 2008. Strain localization in the Morcles nappe (Helvetic alps, Switzerland). Swiss J. Geosci. 101, 341-360.

Bearth, P., 1956. Geologische Beobachtungen im Grenzgebiet der Lepontinischen und Penninischen Alpen. Eclogae Geol. Helv. 49, 279-290.

Bearth, P., 1972. Geologischer Atlas der Schweiz 1:25000 Simplon Atlasblatt 61. Schweizerische Geologische Kommission.

Behr, W.M., Platt, J.P., 2011. A naturally constrained stress profile through the middle crust in an extensional terrane. Earth Planet. Sci. Lett. 303, 181.92, doi: 10.1016/j.epsl.2010.11.044.

Bergemann, C.A., Gnos, E., Berger, A., Janots, E., Whitehouse, M.J., (2020. Dating tectonic activity in the Lepontine Dome and Rhone-Simplon Fault regions through hydrothermal monazite-(Ce). Solid Earth, 11(1), 199-222.

Bolognesi, F., Bistacchi, A., 2016. Weakness and mechanical anisotropy of phyllosilicate-rich cataclasites developed after mylonites of a low-angle normal fault (Simplon Line, Western Alps). J. Struct. Geol. 83, 1-12.

Bose, N., Mukherjee, S., 2020. Estimation of deformation temperatures, flow stresses and strain rates from an intra-continental shear zone: the Main Boundary Thrust, NW Himalaya (Uttarakhand, India). Mar. Pet. Geol. 112, 104094, doi: https://doi.org/10.1016/j.marpetgeo.2019.104094

Caby, R., Pêcher, A., Le Fort, P., 1983. Le grand chevauchement central himalayen: Nouvelles données sur le métamorphisme inverse à la base de la Dalle du Tibet. Revue de Géologie Dynamique et de Géographie Physique, 24, 89–100.

Campani, M., Herman, F., Mancktelow, N.S., 2010b. Two- and three-dimensional thermal modeling of a low-angle detachment: exhumation history of the Simplon Fault Zone, central Alps. J. Geophys. Res. 115, B10420. http://dx.doi.org/10.1029/2009JB007036.

Campani, M., Mancktelow, N., Courrioux, G., 2014. The 3D interplay between folding and faulting in a syn-orogenic extensional system: The Simplon Fault Zone in the central Alps (Switzerland and Italy). Swiss J. Geosci. 107, 251-271. https://doi.org/10.1007/s00015-014-0163-y

Campani, M., Mancktelow, N.S., Seward, D., Rolland, Y., Müller, W., Guerra, I., 2010a. Geochronological evidence for continuous exhumation through the ductile brittle transition along a crustal-scale low-angle normal fault: Simplon Fault Zone, central Alps. Tectonics 29, TC3002. http://dx.doi.org/10.1029/2009TC002582.

Carosi, R., Lombardo, B., Molli, G., Musumeci, G., Pertusati, P.C., 1998. The south Tibetan detachment system in the Rongbuk valley, Everest Region. Deformation features and geological implication. J. Asian Earth Sci. 16, 299–311.

Cawood, T.K., Platt, J.P., 2020. Variations in the PTt of Deformation in a Crustal-Scale Shear Zone in Metagranite. Geochemistry, Geophys. Geosystems. 21, e2020GC009384. https://doi.org/10.1029/2020GC009384

Ceccato, A., Menegon, L., Pennacchioni, G., Morales, L.F.G., 2018. Myrmekite and strain weakening in granitoid mylonites. Solid Earth, 9(6), 1399-1419.

Collettini, C., De Paola, N., Holdsworth, R.E., Barchi, M.R., 2006. The development and behaviour of low-angle normal faults during Cenozoic asymmetric extension in the Northern Apennines, Italy. J. Struct. Geol. 28, 333-352. http://dx.doi.org/10.1016/j.jsg.2005.10.003.

Collettini, C., Holdsworth, R.E., 2004. Fault zone weakening processes along low-angle normal faults: Insights from the Zuccale Fault, Elba, Italy. J. Geol. Soc. 161, 1039-1051. https://doi.org/10.1144/0016-764903-179.

Davis, G.A., Lister, G.S., 1988. Detachment faulting in continental extension: perspectives from the southwestem U.S. Cordillera, Spec. Pep. Geol. Soc. Am., 218, 133-159.

Elfert, S., Reiter, W., Spiegel, C. 2013. Long-lasting tectonic activities of the Lepontine Dome. New evidence from low-temperature thermochronology. Tectonophysics 608, 222-236.

Fossen, H., 2010. Structural geology. Cambridge University Press.

Fossen, H., Cavalcante, G.C.G., 2017. Shear zones–A review. Earth-Sci. Rev. 171, 434-455.

Ghosh, S., Bose, S., Mandal, N., Dasgupta, S., 2016. Dynamic recrystallization mechanisms and their transition in the Daling Thrust (DT) zone, Darjeeling Himalaya. Tectonophysics 674, 166–181.

Gillam, B.G., Little, T.A., Smith, E., Toy, V.G., 2013. Extensional shear band development on the outer margin of the Alpine mylonite zone, Tatare Stream, Southern Alps, New Zealand. J. Struct. Geol. 54, 1-20.

Grasemann, B., Mancktelow, N.S., 1993. Two-dimensional thermal modelling of normal faulting: the Simplon Fault Zone, Central Alps, Switzerland. Tectonophysics 225, 155-165. http://dx.doi.org/10.1016/0040-1951(93)90277-Q.

Graziani, R., Montomoli, C., Iaccarino, S., Menegon, L., Nania, L., Carosi, R., 2020. Structural setting of a transpressive shear zone: insights from geological mapping, quartz petrofabric and kinematic vorticity analysis in NE Sardinia (Italy). Geol. Mag. 157(11), 1898-1916.

Grosjean, G.G., Sue, C., Burkhard, M., 2004. Late Neogene extension in the vicinity of the Simplon fault zone (central Alps, Switzerland). Eclogae Geol. Helv. 97, 33-46. http://dx.doi.org/10.1007/s00015-004-1114-9.

Guidotti, C.V., Sassi, F.P., 1998. Miscellaneous isomorphous substitutions in Na-K white micas: a review, with special emphasis to metamorphic micas. Rend. Lincei Sci. Fis. Nat. 9, 57-78.

Hacker, B.R., Yin, A., Christie, J.M., Snoke, A.W., 1990. Differential stress, strain rate, and temperatures of mylonitization in the Ruby Mountains, Nevada: implications for the rate and duration of uplift. J. Geophys. Res. Solid Earth 95(B6), 8569-8580.

Hacker, B.R., Yin, A., Christie, J.M., Davis, G.A., 1992. Stress magnitude, strain rate, and rheology of extended middle continental crust inferred from quartz grain sizes in the Whipple Mountains, California. Tectonics, 11(1), 36-46.

Haertel, M., Herwegh, M., 2014. Microfabric memory of vein quartz for strain localization in detachment faults: A case study on the Simplon fault zone. J. Struct. Geol. 68, 16-32.

Haertel, M., Herwegh, M., Pettke, T., 2013. Titanium-in-quartz thermometry on synkinematic quartz veins in a retrograde crustal-scale normal fault zone. Tectonophysics 608, 468-481.

Hirth, G., Teyssier, C., Dunlap, J.W., 2001. An evaluation of quartzite flow laws based on comparisons between experimentally and naturally deformed rocks. Int. J. Earth Sci. 90, 77-87. https://doi.org/10.1007/s005310000152.

Holyoke, C.W., Kronenberg, A.K., 2010. Accurate differential stress measurement using the molten salt cell and solid salt assemblies in the Griggs apparatus with applications to strength, piezometers and rheology. Tectonophysics 494, 17-31. https://doi.org/10.1016/j.tecto.2010.08.001.

Hunziker, J.C., Bearth, P., 1969. Rb-Sr-Altersbestimmungen aus den Walliser Alpen: Biotitalterswerte und ihre Bedeutung für die Abkühlungsgeschichte der alpinen Metamorphose. Eclogae Geol. Helv. 62, 205-222.

Iaccarino, S., Montomoli, C., Carosi, R., Montemagni, C., Massonne, H.-J., Langone, A., Jain, A.K., Visonà, D. 2017. Pressure-Temperature-Deformation-Time constraints on the South Tibetan Detachment System in Garhwal Himalaya (NW India). Tectonics, 36, 2281-2304.

Iacopini, D., Frassi, C., Carosi, R., Montomoli, C., 2011. Biases in three-dimensional vorticity analysis using porphyroclast system: limits and application to natural examples. Geol. Soc. London Spec. Publ. 360, 301-318.

Jessup, M. J., Law, R.D., Frassi, C., 2007. The rigid grain net (RGN): an alternative method for estimating mean kinematic vorticity number (Wm). J. Struct. Geol. 29, 411-421.

Johnson, S.E., Lenferink, H.J., Price, N.A., Marsh, J.H., Koons, P.O., West Jr, D.P., Beane, R., 2009. Clast-based kinematic vorticity gauges: the effects of slip at matrix/clast interfaces. J. Struct. Geol. 31(11), 1322-1339.

Keller, L.M., Fügenschuh, B., Hess, M., Schneider, B., Schmid, S.M., 2006. Simplon fault zone in the western and central alps: mechanism of Neogene faulting and folding revisited. Geology 34 (4), 317-320.

Keller, L.M., Hess, M., Fügenschuh, B., Schmid, S.M., 2005. Structural and metamorphic evolution of the Camughera e Moncucco, Antrona and Monte Rosa units southwest of the Simplon line, Western Alps. Eclogae Geol. Helv. 98, 19-49.

Kurz, G.A., Northrup, C.J., 2008. Structural analysis of mylonitic rocks in the Cougar Creek Complex, Oregon–Idaho using the porphyroclast hyperbolic distribution method, and potential use of SC'-type extensional shear bands as quantitative vorticity indicators. J. Struct. Geol. 30, 1005–1012. https://doi.org/10.1016/j.jsg.2008.04.003.

Law, R.D., 2010. Moine Thrust zone mylonites at the Stack of Glencoul: II-results of vorticity analyses and their tectonic significance. Geol. Soc. London Spec. Publ. 335(1), 579-602.

Law, R.D., Searle, M.P., Simpson, R.L., 2004. Strain, deformation temperatures and vorticity of flow at the top of the Greater Himalayan Slab, Everest Massif, Tibet. J. Geol. Soc. 161, 305–320.

Law, R.D., Stahr, D.W., Francsis, M.K., Ashley, K.T., Grasemann, B., Ahmad, T., 2013. Deformation temperatures and flow vorticities near the base of the Greater Himalayan Series, Sutlej Valley and Shimla Klippe, NW India. J. Struct. Geol. 54, 21–53.

Lister, G.S., 1977. Discussion: crossed-girdle c-axis fabrics in quartzites plastically deformedby plane strain and progressive simple shear. Tectonophysics, 39, 51-54.

Lister, G.S., Paterson, M.S., 1979. The simulation of fabric development during plastic deformation and its application to quartzite: Fabric transitions. J. Struct. Geol. 1, 99-115.

Malvern, L.E., 1969. Introduction to Mechanics of a Continuous Medium. Prentice Hall, New Jersey.

Mancel, P., Merle, O., 1987. Kinematics of the northern part of the Simplon line (Central Alps). Tectonophysics 135 (4), 265-275.

Mancktelow, N.S., 1985. The Simplon Line: a major displacement zone in the western Lepontine Alps. Eclogae Geol. Helv. 78, 73-96.

Mancktelow, N.S., 1987a. Atypical textures in quartz veins from the Simplon fault zone. J. Struct. Geol. 9 (8), 995-1005.

Mancktelow, N.S., 1987b. Quartz textures from the Simplon fault zone, southwest Switzerland and north Italy. Tectonophysics 135, 133-153.

Mancktelow, N.S., 1990. The Simplon Fault Zone. Beitrage zur Geologischen Karte der Schweiz.

Mancktelow, N.S., 1992. Neogene lateral extension during convergence in the Central Alps: evidence from interrelated faulting and backfolding around the Simplonpass (Switzerland). Tectonophysics 215, 295-317. http://dx.doi.org/10.1016/0040-1951(92)90358-D.

Massironi, M., Bistacchi, A., Menegon, L., 2011. Misoriented faults in exhumed metamorphic complexes: rule or exception? Earth Planet. Sci. Lett. 307, 233-239. http://dx.doi.org/10.1016/j.epsl.2011.04.041.

Means,W.D.,1981. The concept of steady-state foliation. Tectonophysics 78,179-199.

Means,W.D.,1995. Shear zones and rock history. Tectonophysics 247 (1-4),157-160.

Menegon, L., Nasipuri, P., Stünitz, H., Behrens, H., Ravna, E., 2011. Dry and strong quartz during deformation of the lower crust in the presence of melt. J. Geophys. Res. Solid Earth 116. doi: 10.1029/2011JB008371.

Menegon, L., Pennacchioni, G., Heilbronner, R., Pittarello, L., 2008. Evolution of quartz microstructure and c-axis crystallographic preferred orientation withinductilely deformed granitoids (Arolla unit, Western Alps). J. Struct. Geol. 30, 1332-1347.

Merle, P.O., Le Gal, P., Mancel, P., 1986. Deformation et metamorphisme dans la region du Simplon (Alpes centrales). Eclogae Geol. Helv. 79 (3), 705-718.

Montemagni, C., Carosi, R., Fusi, N., Iaccarino, S., Montomoli, C., Villa, I.M., Zanchetta, S. 2020. Three-dimensional vorticity and time-constrained evolution of the Main Central Thrust zone, Garhwal Himalaya (NW India). Terra Nova 32, 215–224, https://doi.org/https://doi.org/10.1111/ter.12450

Montemagni, C., Villa, I.M. 2021. Geochronology of Himalayan shear zones: unravelling the timing of thrusting from structurally complex fault rocks. J. Geol. Soc. doi: https://doi.org/10.1144/jgs2020-235.

Müller, W., Kelley, S.P., Villa, I.M., 2002. Dating fault-generated pseudotachylytes: Comparison of ^{40}Ar/^{39}Ar stepwise-heating, laser-ablation and Rb-Sr microsampling analyses. Contrib. Mineral. Petrol. 144, 57-77.

Oriolo, S., Oyhantçabal, P., Wemmer, K., Heidelbach, F., Pf˙ander, J., Basei, M.A.S., Hueck, M., Hannich, F., Sperner, B., Siegesmund, S., 2016. Shear zone evolution and timing of deformation in the Neoproterozoic transpressional Dom Feliciano Belt, Uruguay. J. Struct. Geol. 92, 59-78. https://doi.org/10.1016/j.jsg.2016.09.010.

Oriolo, S., Wemmer, K., Oyhantçabal, P., Fossen, H., Schulz, B., Siegesmund, S., 2018. Geochronology of shear zones – a review. Earth Sci. Rev. 185, 665-683. https://doi. org/10.1016/j.earscirev.2018.07.007.

Passchier, C.W., 1987. Stable position of rigid objects in noncoaxial flow: a study in vorticity analysis. J. Struct. Geol. 9, 679-690.

Passchier, C.W., Trouw, R.A.J., 2005. Microtectonics. Berlin: Springer Verlag.

Pennacchioni, G., Menegon, L., Leiss, B., Nestola, F., Bromiley, G., 2010. Development of crystallographic preferred orientation and microstructure during plastic deformation of natural coarse- grained quartz veins. J. Geophys. Res. Solid Earth, 115(B12).

Peternell, M., Hasalová, P., Wilson, C. J., Piazolo, S., Schulmann, K., 2010. Evaluating quartz crystallographic preferred orientations and the role of deformation partitioning using EBSD and fabric analyser techniques. J. Struct. Geol. 32, 803-817.

Pitzer, K.S., Sterner, S.M., 1994. Equation of state valid continuously from zero to extreme pressures for H_2O and CO_2. J. Chem. Phys. 101, 3111-3116.

Pryer, L.L., 1993. Microstructures in feldspars from a major crustal thrust zone: the Grenville Front, Ontario, Canada. J. Struct. Geol. 15, 21-36.

Ramsay, J.G., 1980. Shear zone geometry: a review. J. Struct. Geol. 2, 83-99.

Rosenberg, C.L., Schneider, S., Scharf, A., Bertrand, A., Hammerschmidt, K., Rabaute, A., Brun, J. P., 2018. Relating collisional kinematics to exhumation processes in the Eastern Alps. Earth- Sci. Rev. 176, 311-344.

Rudnick, R.L., Gao, S., 2003. Composition of the Continental Crust. R.L. Rudnick (Ed.), Treatise of Geochemistry, v. 3, The Crust, Elsevier, 1-64.

Sanchez, G., Rolland, Y., Schneider, J., Corsini, M., Oliot, E., Goncalves, P., Verati, C., Lardeaux, J.-M., Marquer, D., 2011. Dating low-temperature deformation by $^{40}Ar/^{39}Ar$ on white mica, insights from the Argentera-Mercantour Massif (SW Alps). Lithos, 125, 521-536.

Scharf, A., Handy, M.R., Schmid, S.M., Favaro, S., Sudo, M., Schuster, R., Hammerschmidt, K., 2016. Grain-size effects on the closure temperature of white mica in a crustal-scale extensional shear zone—Implications of in-situ $^{40}Ar/^{39}Ar$ laser-ablation of white mica for dating shearing and cooling (Tauern Window, Eastern Alps). Tectonophysics 674, 210-226.

Schmid, S.M., Casey, M., 1986. Complete fabric analysis of some commonly observed quartz c-axis patterns. In: Hobbs, B.E., Heard, H.C. (Eds.), Mineral and Rock Deformation: Laboratory Studies - The Paterson Volume. American Geophysical Union Monograph, 36. American Geophysical Union, 246-261.

Schoene, B., Bowring, S.A., 2006. U–Pb systematics of the McClure Mountain syenite: thermochronological constraints on the age of the $^{40}Ar/^{39}Ar$ standard MMhb. Contrib. Mineral. Petrol. 151, 615-630.

Sibson, R.H., 1977. Fault rocks and fault mechanisms. J. Geol. Soc. 133(3), 191-213.

Simonetti, M., Carosi, R., Montomoli, C., Law, R.D., Cottle, J.M., 2021. Unravelling the development of regional-scale shear zones by a multidisciplinary approach: the case study of the

Ferriere-Mollières Shear Zone (Argentera Massif, Western Alps). J. Struct. Geol. 104399, doi: https://doi.org/10.1016/j.jsg.2021.104399.

Steck, A., 1987. Le massif du Simplon e reflexions sur la cinematique des nappes de gneiss. Schweiz. Mineral. Petrogr. Mittl. 67, 27-45.

Steck, A., 2008. Tectonics of the Simplon massif and Lepontine gneiss dome: deformation structures due to collision between the underthrusting European plate and the Adriatic indenter. Swiss J. Geosci. 101, 515-546. http://dx.doi.org/10.1007/s00015-008-1283-z.

Steck, A., Hunziker, J., 1994. The Tertiary structural and thermal evolution of the Central Alps e compressional and extensional structures in an orogenic belt. Tectonophysics 238, 229-254.

Steck, A., 1990. A map of ductile shear zones of the Central Alps. Eclogae Geol. Helv. 83 (3), 603-627.

Stipp, M., Stunitz, H., Heilbronner, R., Schmid, S.M., 2002. The eastern Tonale fault zone: A natural laboratory for crystal plastic deformation over a temperature range from 250 to 700 °C. J. Struct. Geol. 24, 1861–1884.

Stipp, M., Tullis, J., 2003. The recrystallized grain size piezometer for quartz. Geophys. Res. Lett. 30 (21), 3.1-3.5.

Stipp, M., Tullis, J., Scherwath, M., Behrmann, J.H., 2010. A new perspective on paleopiezometry: dynamically recrystallized grain size distributions indicate mechanism changes. Geology 38 (8), 759–762. https://doi.org/10.1130/G31162.1.

Studer, B., 1851: Geologie der Schweiz. Stämpflische Verlagshandlung Bern und Friedrich Schulthess Zürich.

Toy, V.G., Prior, D.J., Norris, R.J., 2008. Quartz fabrics in the Alpine Fault mylonites: Influence of pre-existing preferred orientations on fabric development during progressive uplift. Journal of Structural Geology, 30(5), 602-621.

Trouw, R. A., Passchier, C.W., Wiersma, D.J., 2010. Atlas of Mylonites-and related microstructures. Springer Science & Business Media.

Vance, D., Müller, W., Villa, I.M., 2003. Geochronology: linking the isotopic record with petrology and textures—an introduction. In: Vance, D., Müller, W., Villa, I.M. (Eds.), Geochronology: Linking the Isotopic Record with Petrology and Textures, Geol. Soc. London Spec. Publ. 220, 1-24.

Villa, I.M., 2016. Diffusion in mineral geochronometers: Present and absent. Chem. Geol. 420, 1-10.

Villa, I.M., Hermann, J., Müntener, O., Trommsdorff, V. 2000. ^{39}Ar–^{40}Ar dating of multiply zoned amphibole generations (Malenco, Italian Alps). Contrib. Mineral. Petrol. 140(3), 363-381.

Wallis, S., 1995. Vorticity analysis and recognition of ductile extension in the Sanbagawa belt, SW Japan. J. Struct. Geol. 17(8), 1077-1093.

Wallis, S.R., Platt, J.P., Knott, S.D., 1993. Recognition of syn-convergence extension in accretionary wedges with examples from the Calabrian arc and the eastern Alps. Am. J. Sci. 293, 463-495.

Wernicke, B., 1981. Low-angle normal faults in the Basin and Range Province: nappe tectonics in an extending orogen. Nature 291, 645-648. http://dx.doi.org/10.1038/291645a0.

Wernicke, B., 2009. The detachment era (1977–1982) and its role in revolutionizing continental tectonics. In: U. Ring & B. Wernicke (Eds.), Extending a Continent: Architecture, Rheology and Heat Budget, Geol. Soc. London Spec. Publ. 321, 1-8. https://doi.org/ 10.1144/SP321.1

Xypolias, P., 2009. Some new aspects of kinematic vorticity analysis in naturally deformed quartzites. J. Struct. Geol. 31, 3–10. https://doi.org/10.1016/j.jsg.2008.09.009.

Xypolias, P., 2010. Vorticity analysis in shear zones: a review of methods and applications. J. Struct. Geol. 32, 2072–2092. https://doi.org/10.1016/j.jsg.2010.08.009.

Figure captions

Fig. 1. Geological setting of the Simplon Fault Zone in the central Alps. (a) Location of the study area is marked with a red box; (b) Sketch map of the Simplon area (modified after Campani et al., 2010a, Cawood and Platt, 2020). AA’ is the trace of cross section of Fig. 3. PFS: Periadriatic Fault System.

Fig. 2. Detailed geological maps of the Simplon Pass area. The original survey was performed at a 1:5000 scale. AA’ represents the trace of cross section of Fig. 3. Equal area, lower hemisphere stereographic projections of main foliation (S_m) and main lineation (L_m) referred to the Berisal and Monte Leone units in the SSZ are reported. AA’ is the trace of the cross section reported in Fig. 3.

Fig. 3. SW- NE cross section. The location of studied samples has been reported.

Fig. 4. Field photographs of calcschist of Monte Leone Unit (a) and garnet-paragneiss of Berisal Unit (b) showing a SC’ fabric clearly pointing to a top-to-SW shear sense. (c) Quartz band in paragneiss of the Berisal Unit frequently occurs in the field. (d) Orthogneiss (Berisal Unit) with an intensively developed SC’ fabric. (e) Transition from mylonite to ultramylonite within a few meters in the field. (f) Orthogneiss with a quartz band (Berisal Unit).

Fig. 5. Representative photomicrographs from the SSZ, crossed polars. (a) and (b) Quartz ribbons in paragneiss (SPL-20) at the top of the SSZ show a well advanced oblique grain shape foliation, indicating a top-to-SW sense of shear. (c) Low-T mylonite *sensu* Cawood and Platt (2020) characterized by fine-grained SGR/BLG recrystallized quartz and micas along C’ planes. (d) Extremely elongated quartz ribbon (yellow arrow) showing evidence of SGR/BLG recrystallization mechanisms in quartz (narrow shear bands of Cawood and Platt, 2020). (e) Clearly developed SC’ fabric in mylonitic orthogneiss (SPL-7) showing a top-to-SW sense of shear; some asymmetric K-feldspar porphyroclasts and synthetic bookshelf structures in K-feldspar porphyroclast (yellow arrow) indicate a top-to-SW shear sense too. (f) SC’ fabric in mylonitic orthogneiss (SPL-3), group-2 mica fishes (Passchier and Trouw, 2005) and tapering deformation twins in K-feldspar. (g) Ribbon of quartz at the bottom of the SSZ (SPL-5) characterized by GBM/SGR recrystallization mechanism and oblique grain shape foliation.

Fig. 6. Quartz CPO fabrics from SSZ from sample SPL-20 (a), SPL-6 (b), SPL-2 (c) and SPL-5 (d). Fabric skeleton (black lines) constructed from contoured *c*-axis plot. Stereonets are equal area lower

hemisphere projections. The *c*-axis plot view is up-foliation and refer as reference frame to the foliation pole (Z) and lineation (X). Colour bar charts indicate multiples of uniform distribution (m.u.d.) of CPO. (e) δ/β nomogram for estimating W_m and R_{XZ} (modified from Xypolias, 2009). Samples are colour-coded referred to main quartz recrystallization mechanisms: green=BLG, blue=SGR, red=GBM. (f) and (g) examples of inverse pole figure maps colour coded with respect to the X direction. The grey-shaded areas are other phases (k-feldspar and plagioclase) or non-indexed points. (h-m) Histograms show grain size distribution. At the right top relationship between the main mylonitic foliation (S_a) and the oblique grain shape fabric (S_b) with long axes of quartz neoblasts nucleating parallel to the extensional ISA_2 (modified from Fossen and Cavalcante, 2017). Quartz *c*-axis fabric diagram: shear plane assumed to be perpendicular to central segment of fabric skeleton (modified from Law et al., 2004).

Fig. 7. Vorticity estimates through SC' (a-b) and RGN (c-d) methods. Polar histograms used to derive the angle θ and to calculate kinematic vorticity with the SC' method (Kurz and Northrup, 2008) for samples SPL-7 (a) and SPL-3 (b). Kinematic vorticity analysis with stable porphyroclasts method presented with Rigid Grain Net graphs (Jessup et al., 2007) for samples SPL-7 (c) and SPL-3 (d). A_1 = flow apophysis 1; A_2 = flow apophysis 2. Dashed line represent the bisector of the angle between A_1 and A_2.

Fig. 8. EPMA results showing compositional variation in muscovite (a-b) and biotite (c-d).

Fig. 9. ^{40}Ar/^{39}Ar age spectra, Ca/K vs. age diagrams and DRPs for samples SPL-8 (a-c), SPL-6 (d-f), SPL-1 (g-i), SPL-3 (l-n) and SPL-4 (o-q).

Fig. 10. (a) Cross section showing the distribution of deformation temperatures related to quartz recrystallization mechanisms and age of syn-mylonitic micas. (b) Summary of data from top to bottom of the shear zone: quartz recrystallization mechanisms, age, kinematic vorticity number, grain size, differential stress and strain rate values. Grain size are expressed as the diameter of the equivalent circle; differential stresses are calculated using the piezometer of Stipp and Tullis (2003) with experimental calibration of Holyoke and Kronenberg (2010). For the strain rate values the water fugacity was calculated using the equation of state of Pitzer and Sterner (1994). RGN: Rigid Grain Net method; C'-SB: C' shear bands method; OGSF: oblique grain shape foliation method.

Supplementary Fig. 1. *a*-axis pole figures of samples selected for oblique grain shape foliation method analysis. Colour bar charts show m.u.d. of CPO.

Supplementary Table captions

Supplementary Table 1. Electron probe micro analyses of micas (wt% oxides). Atomic proportions (apfu) were recalculated based on 11 oxygens.

Supplementary Table 2. ^{40}Ar/^{39}Ar data. All Ar isotope concentrations are given as mL. K, Ca and Cl concentrations are calculated from the sample mass and the ^{39}Ar, ^{37}Ar and ^{38}Ar concentrations, respectively.

Highlights:

. The Simplon Fault Zone accommodated the exhumation of the western Lepontine Dome

. Ductile shearing along the SFZ was still ongoing at 8 Ma

. Simple shear in the SFZ decreases structurally upwards from 88% to 37%

. Differential stress and strain rate are coherent with values obtained in metagranitoids deformed in the mid and upper continental crust

Declaration of interests

☒ The authors declare that they have no known competing financial interests or personal relationships that could have appeared to influence the work reported in this paper.

☐The authors declare the following financial interests/personal relationships which may be considered as potential competing interests:

Chiara Montemagni: Conceptualization, Investigation, Methodology, Formal analysis, Data curation, Writing - original draft, Writing - review & editing

Stefano Zanchetta: Conceptualization, Investigation, Formal analysis, Funding acquisition, Project administration, Resources, Supervision, Writing - review & editing

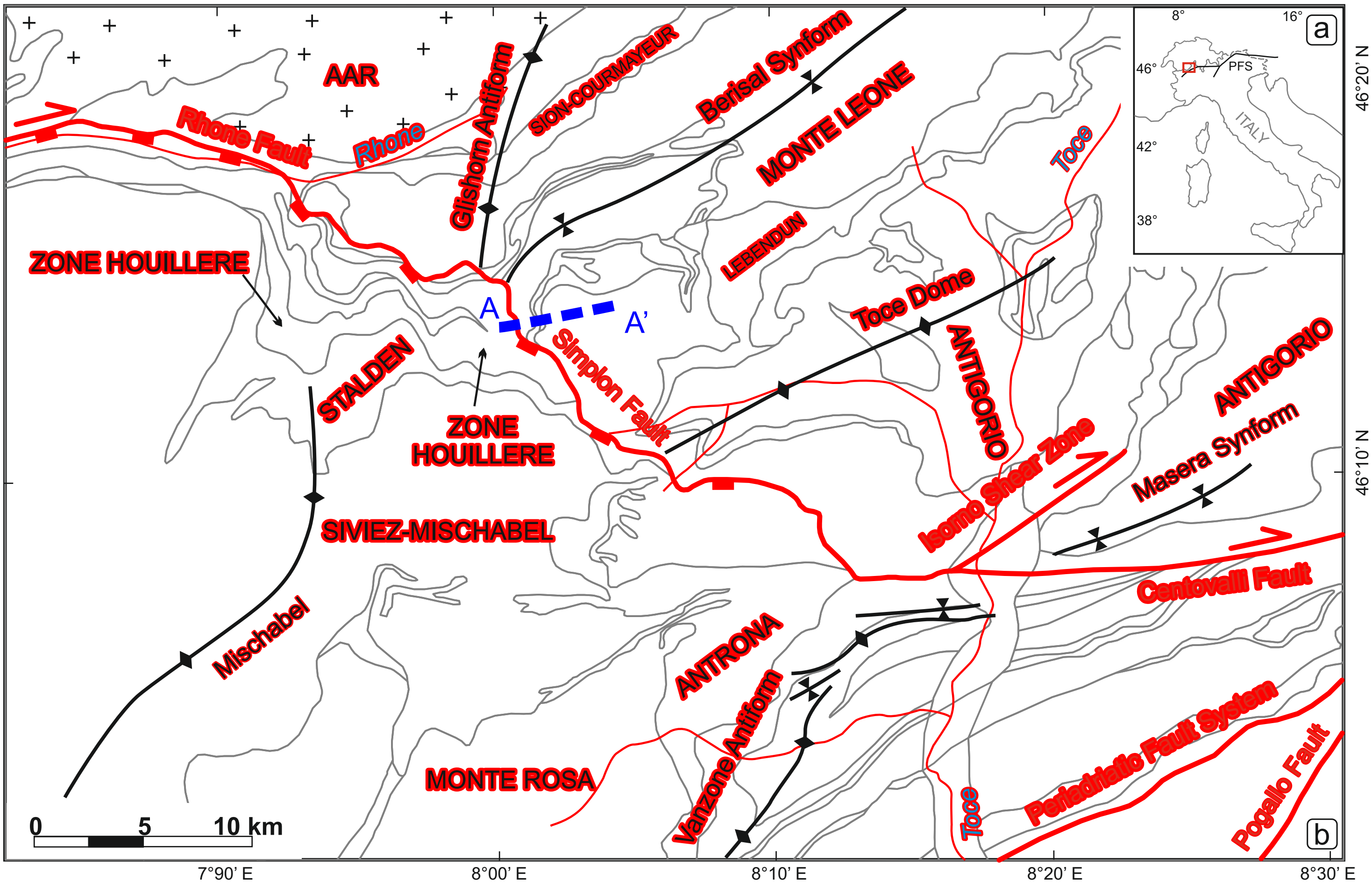

Fig. 1. Geological setting of the Simplon Fault Zone in the central Alps. (a) Location of the study area is marked with a red box; (b) Sketch map of the Simplon area (modified after Campani et al., 2010a, Cawood and Platt, 2020). AA' is the trace of cross section of Fig. 3. PFS: Periadriatic Fault System.

Figure 2

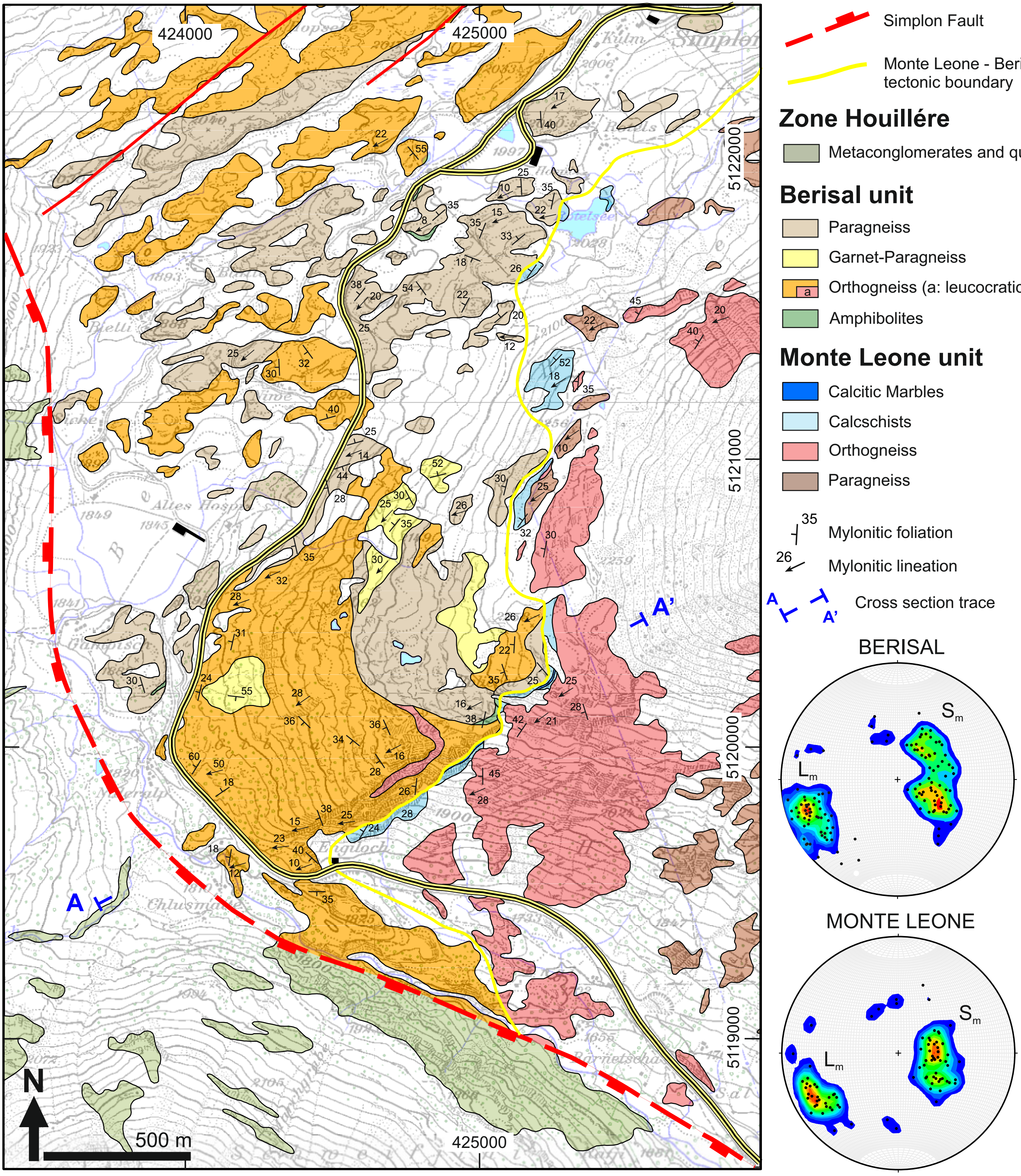

Fig. 2. Detailed geological maps of the Simplon Pass area. The original survey was performed at a 1:5000 scale. AA' represents the trace of cross section of Fig. 3. Equal area, lower hemisphere stereographic projections of main foliation (S_m) and main lineation (L_m) referred to the Berisal and Monte Leone units in the SSZ are reported. AA' is the trace of the cross section reported in Fig. 3.

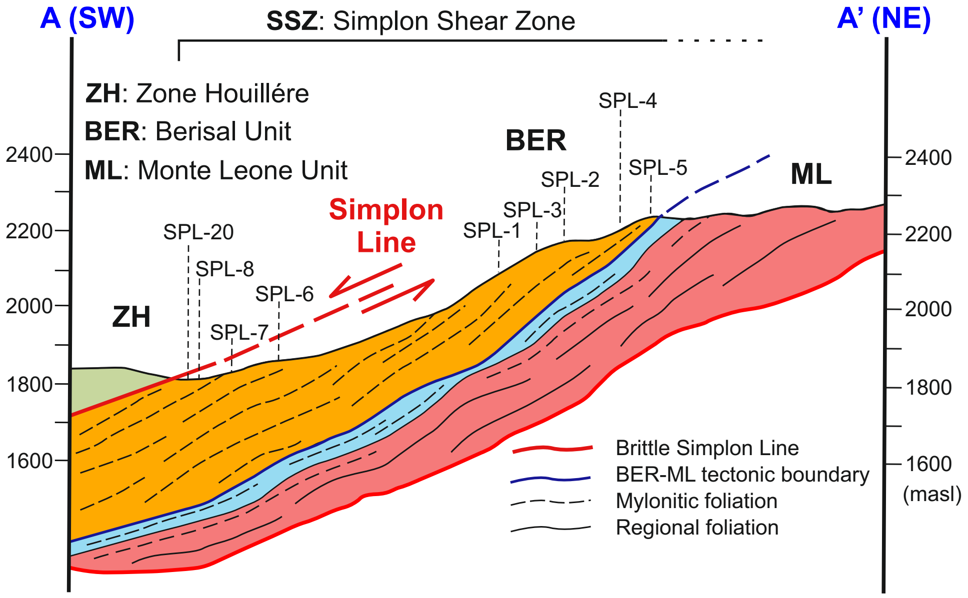

Fig. 3. SW-NE cross section. The location of studied samples has been reported.

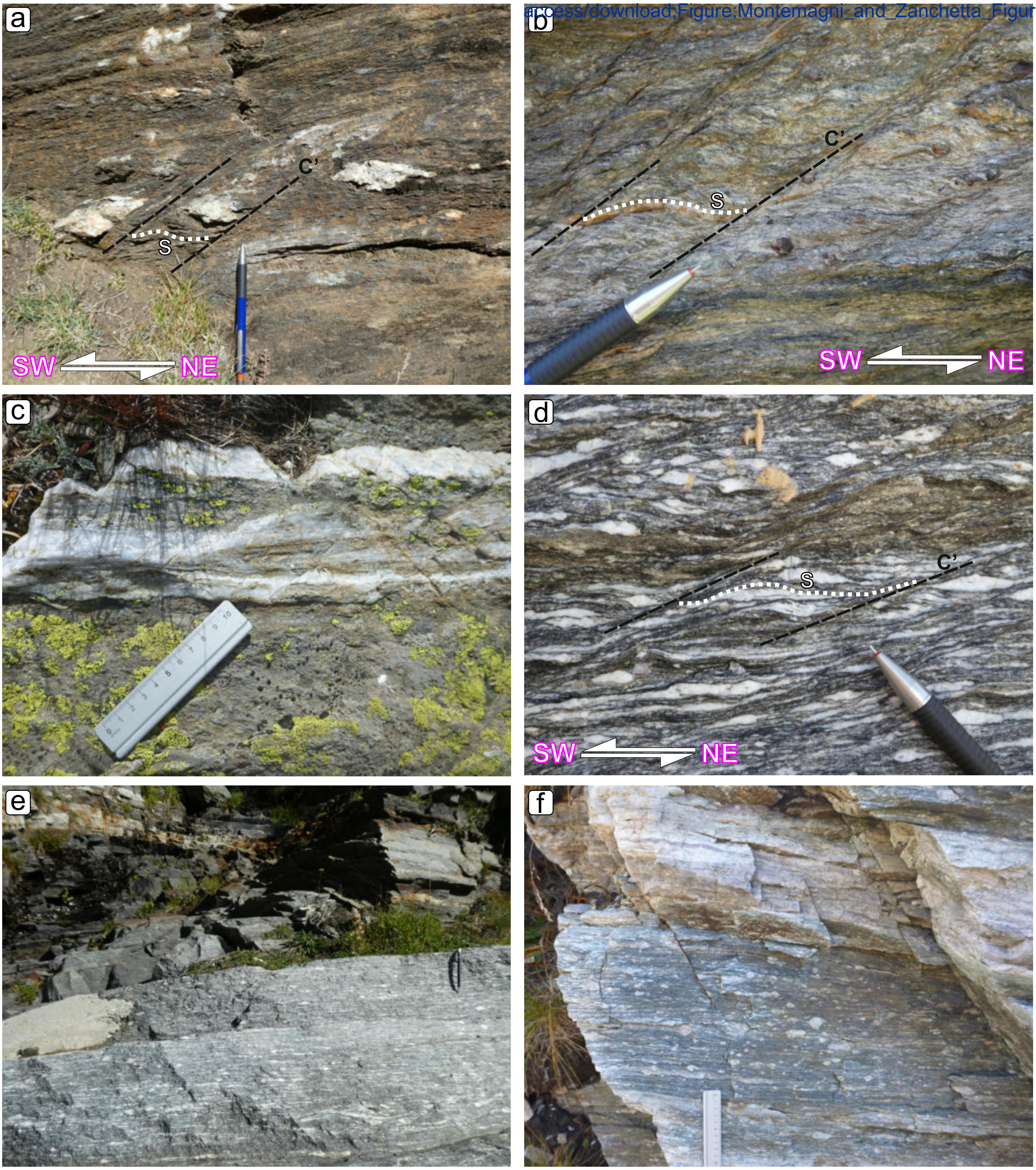

Fig. 4. Field photographs of calcschist of Monte Leone Unit (a) and garnet-paragneiss of Berisal Unit (b) showing a SC' fabric clearly pointing to a top-to-SW shear sense. (c) Quartz band in paragneiss of the Berisal Unit frequently occurs in the field. (d) Orthogneiss (Berisal Unit) with an intensively developed SC' fabric. (e) Transition from mylonite to ultramylonite within a few meters in the field. (f) Orthogneiss with a quartz band (Berisal Unit).

Figure 5

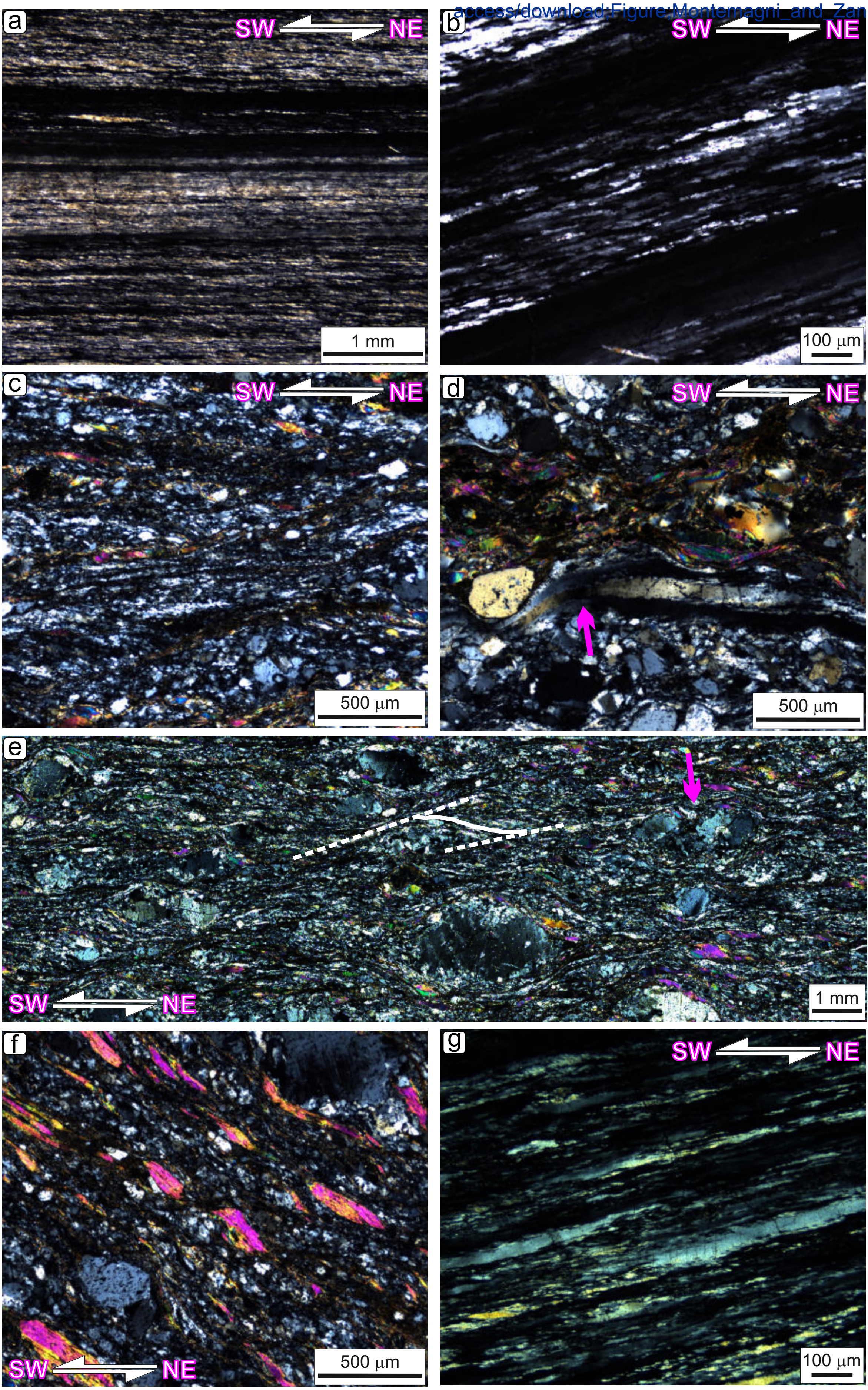

Fig. 5. Representative photomicrographs from the SSZ, crossed polars. (a) and (b) Quartz ribbons in paragneiss (SPL-20) at the top of the SSZ show a well advanced oblique grain shape foliation, indicating a top-to-SW sense of shear. (c) Low-T mylonite *sensu* Cawood and Platt (2020) characterized by fine-grained SGR/BLG recrystallized quartz and micas along C' planes. (d) Extremely elongated quartz ribbon (yellow arrow) showing evidence of SGR/BLG recrystallization mechanisms in quartz (narrow shear bands of Cawood and Platt, 2020). (e) Clearly developed SC' fabric in mylonitic orthogneiss (SPL-7) showing a top-to-SW sense of shear; some asymmetric K-feldspar porphyroclasts and synthetic bookshelf structures in K-feldspar porphyroclast (yellow arrow) indicate a top-to-SW shear sense too. (f) SC' fabric in mylonitic orthogneiss (SPL-3), group-2 mica fishes (Passchier and Trouw, 2005) and tapering deformation twins in K-feldspar. (g) Ribbon of quartz at the bottom of the SSZ (SPL-5) characterized by GBM/SGR recrystallization mechanism and oblique grain shape foliation.

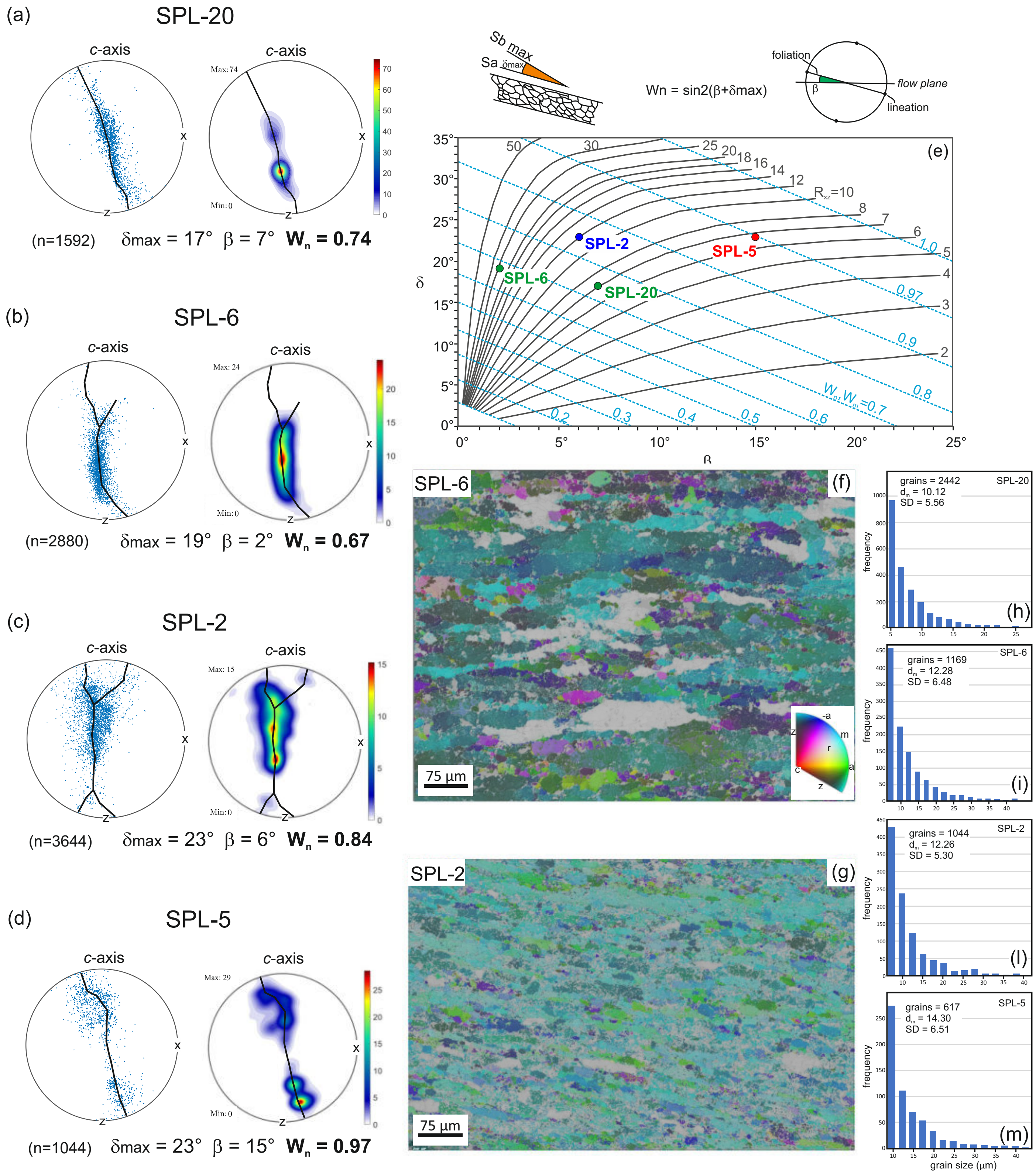

Fig. 6. Quartz CPO fabrics from SSZ from sample SPL-20 (a), SPL-6 (b), SPL-2 (c) and SPL-5 (d). Fabric skeleton (black lines) constructed from contoured *c*-axis plot. Stereonets are equal area lower hemisphere projections. The *c*-axis plot view is up-foliation and refer as reference frame to the foliation pole (Z) and lineation (X). Colour bar charts indicate multiples of uniform distribution (m.u.d.) of CPO. (e) δ/β nomogram for estimating W_m and R_{XZ} (modified from Xypolias, 2009). Samples are colour-coded referred to main quartz recrystallization mechanisms: green=BLG, blue=SGR, red=GBM. (f) and (g) examples of inverse pole figure maps colour coded with respect to the X direction. The grey-shaded areas are other phases (k-feldspar and plagioclase) or non-indexed points. (h-m) Histograms show grain size distribution. At the right top relationship between the main mylonitic foliation (S_a) and the oblique grain shape fabric (S_b) with long axes of quartz neoblasts nucleating parallel to the extensional ISA_2 (modified from Fossen and Cavalcante, 2017). Quartz *c*-axis fabric diagram: shear plane assumed to be perpendicular to central segment of fabric skeleton (modified from Law et al., 2004).

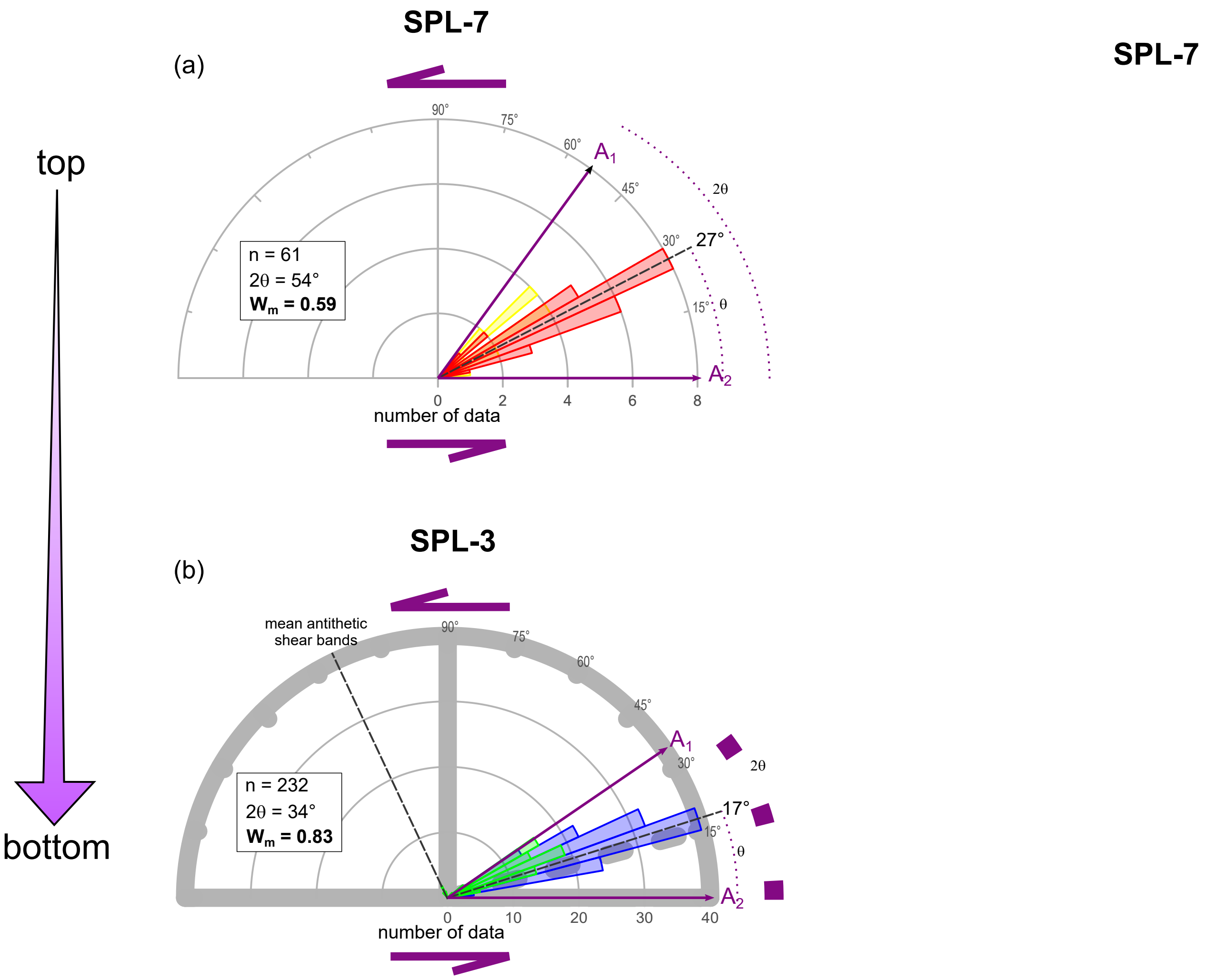

Fig. 7. Vorticity estimates through SC' (a-b) and RGN (c-d) methods. Polar histograms used to derive the angle θ and to calculate kinematic vorticity with the SC' method (Kurz and Northrup, 2008) for samples SPL-7 (a) and SPL-3 (b). Kinematic vorticity analysis with stable porphyroclasts method presented with Rigid Grain Net graphs (Jessup et al., 2007) for samples SPL-7 (c) and SPL-3 (d). A1 = flow apophysis 1; A2 = flow apophysis 2. Dashed line represent the bisector of the angle between A1 and A2.

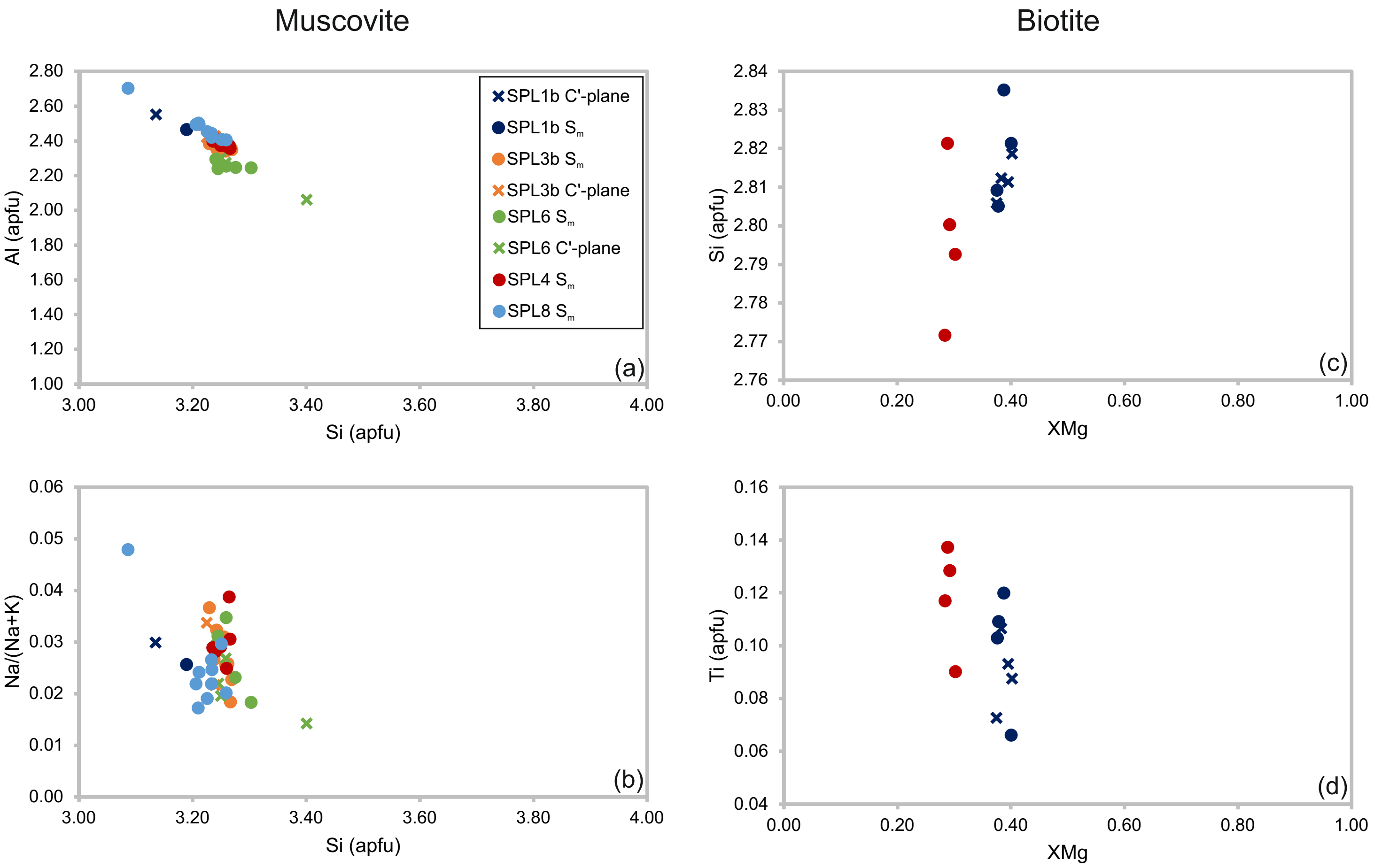

Fig. 8. EPMA results showing compositional variation in muscovite (a-b) and biotite (c-d).

Figure 9

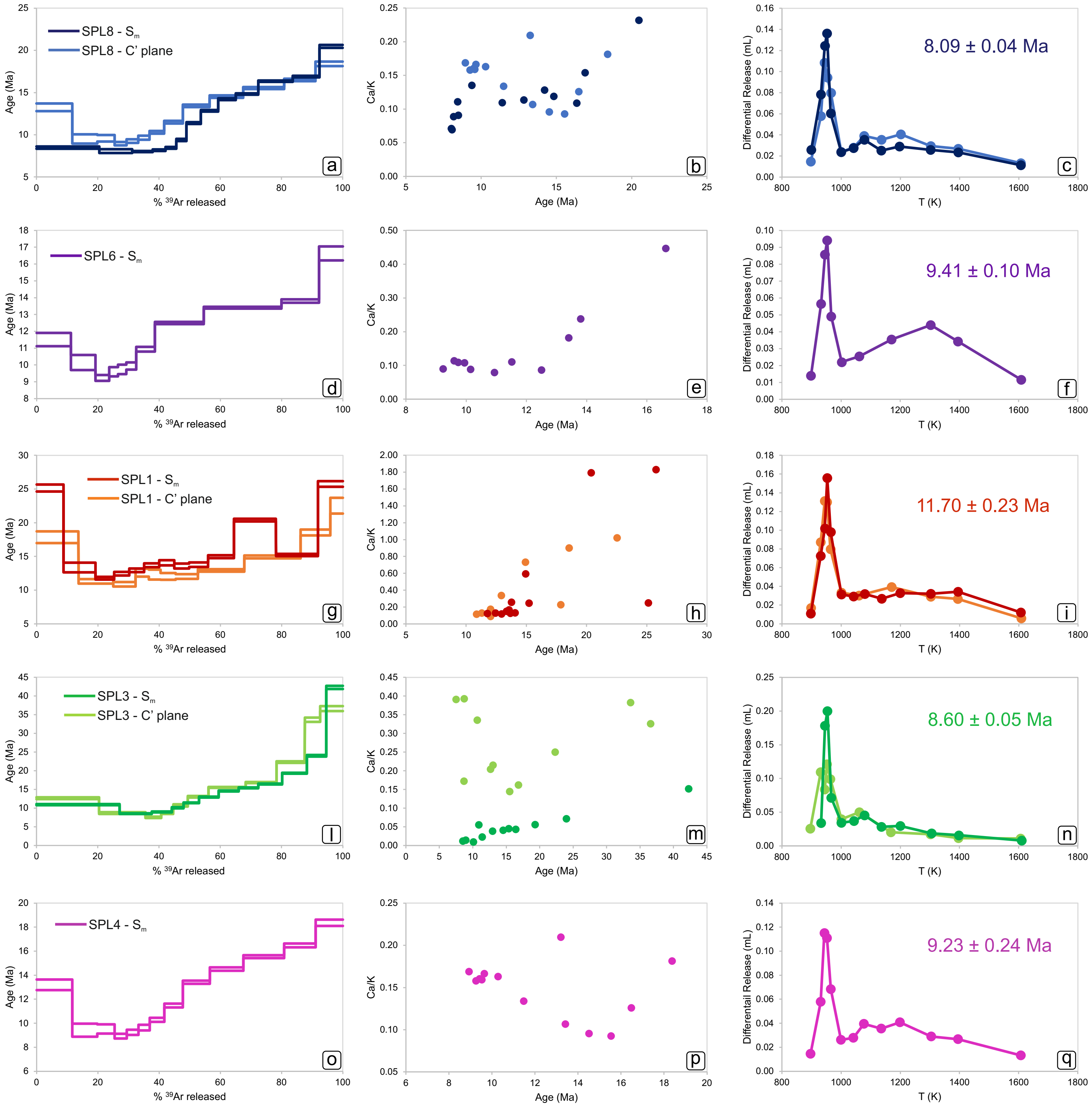

Fig. 9. ^{40}Ar/^{39}Ar age spectra, Ca/K vs. age diagrams and DRPs for samples SPL-8 (a-c), SPL-6 (d-f), SPL-1 (g-i), SPL-3 (l-n) and SPL-4 (o-q).

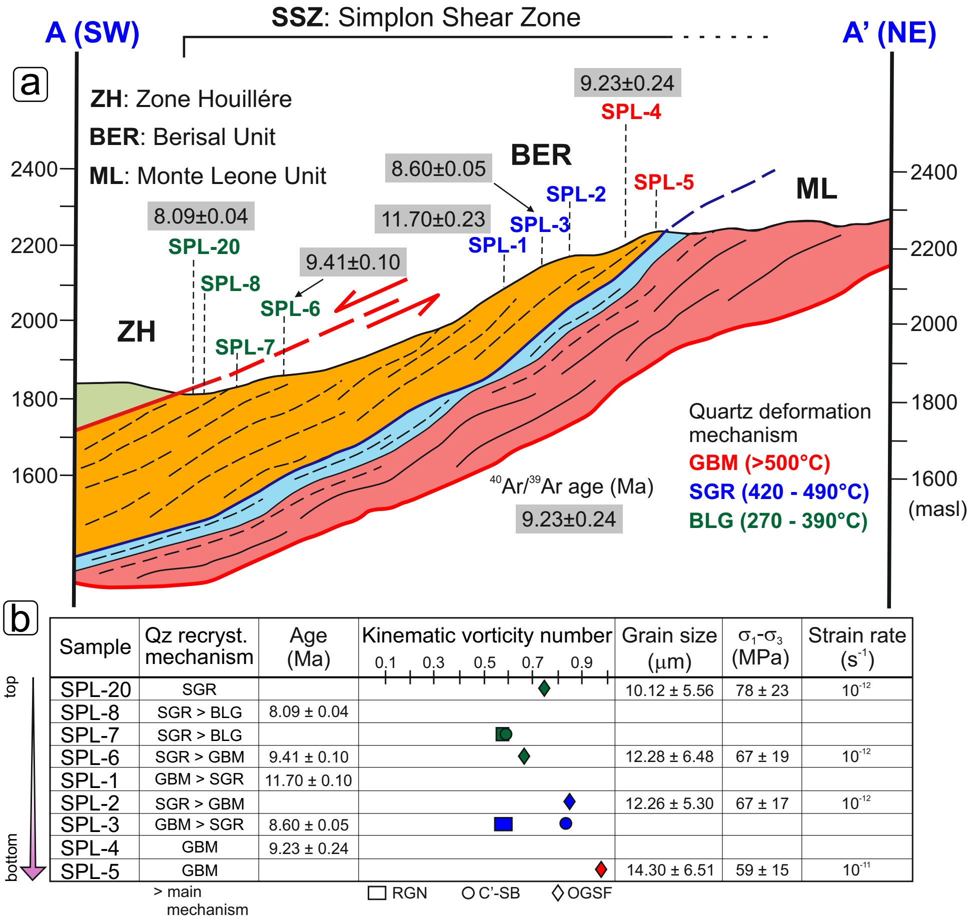

Sample	Qz recryst. mechanism	Age (Ma)	Kinematic vorticity number	Grain size (μm)	σ_1-σ_3 (MPa)	Strain rate (s^{-1})
SPL-20	SGR		◆	10.12 ± 5.56	78 ± 23	10^{-12}
SPL-8	SGR > BLG	8.09 ± 0.04				
SPL-7	SGR > BLG		■●			
SPL-6	SGR > GBM	9.41 ± 0.10	◆	12.28 ± 6.48	67 ± 19	10^{-12}
SPL-1	GBM > SGR	11.70 ± 0.10				
SPL-2	SGR > GBM		◆	12.26 ± 5.30	67 ± 17	10^{-12}
SPL-3	GBM > SGR	8.60 ± 0.05	■ ●			
SPL-4	GBM	9.23 ± 0.24				
SPL-5	GBM		◆	14.30 ± 6.51	59 ± 15	10^{-11}

Fig. 10. (a) Cross section showing the distribution of deformation temperatures related to quartz recrystallization mechanisms and age of syn-mylonitic micas. (b) Summary of data from top to bottom of the shear zone: quartz recrystallization mechanisms, age, kinematic vorticity number, grain size, differential stress and strain rate values. Grain size are expressed as the diameter of the equivalent circle; differential stresses are calculated using the piezometer of Stipp and Tullis (2003) with experimental calibration of Holyoke and Kronenberg (2010). For the strain rate values the water fugacity was calculated using the equation of state of Pitzer and Sterner (1994). RGN: Rigid Grain Net method; C'-SB: C' shear bands method; OGSF: oblique grain shape foliation method.

Supplementary Figure 1

Supplementary Table 1

Supplementary Table 2